

1 **Incongruent chemical weathering and adsorption of neodymium drive modulation**
2 **of neodymium isotope composition of global riverine particulate matter**

3 Anup Kumar Sharma^{1*}, Tarun Kumar Dalai^{1*}, Prem Chand Kisku², Jitendra Kumar Pattanaik³,
4 Sambuddha Misra⁴, Shivansh Verma⁵, Anil Dutt Shukla^{5,6}

5
6
7 ¹Department of Earth Sciences, Indian Institute of Science Education and Research Kolkata, Mohanpur 741246, India

8 ²Council of Scientific and Industrial Research-National Geophysical Research Institute (CSIR-NGRI), Uppal Road,
9 Hyderabad 500007, India

10 ³Department of Geology, Central University of Punjab, Bathinda, Punjab 151401, India

11 ⁴Centre for Earth Sciences, Indian Institute of Science, Bangalore 560012, India

12 ⁵Geosciences Division, Physical Research Laboratory, Ahmedabad 380009, India

13 ⁶Department of Geology, HNB Garhwal University, Srinagar, Uttarakhand 246174, India

14 *Authors for correspondence: (aks18rs032@iiserkol.ac.in, dalai@iiserkol.ac.in)

15
16
17
18
19
20
21

22 **This manuscript is a preprint (non-peer reviewed)** on EarthArXiv and has been submitted for
23 consideration in Earth and Planetary Science Letters (EPSL). Please be aware that future versions of this
24 manuscript may include updates or revisions.

Abstract

25
26 We report incongruent weathering and differential release of radiogenic neodymium (^{143}Nd) to challenge
27 the widely accepted congruent behaviour of Nd isotopes during weathering of rocks. Investigating two
28 basaltic weathering profiles of the Rajmahal Volcanic Province in India, the incongruent behaviour of
29 minerals and Nd isotopes were established. These results contradict the premise of invariant nature of
30 $^{143}\text{Nd}/^{144}\text{Nd}$ (expressed as ϵ_{Nd}) during surface processes, the basis for extensive application of ϵ_{Nd} in
31 geological and geochemical studies. We also demonstrate that the ϵ_{Nd} of Nd released to the weathering
32 solution is reliably captured by the oxyhydroxide phases of the weathering profiles. Combining these
33 two observations, we hypothesize that riverine particulate ϵ_{Nd} is sensitive to adsorption of dissolved Nd
34 and would be regulated by the duration of water-particle interaction during transport. Therefore, we
35 predict that particulate ϵ_{Nd} would be different between the high and low discharge periods in a river
36 catchment.

37 Utilising published results of fourteen rivers from across the world, which cover multiple
38 lithologies and climatic regimes, we demonstrate that differential release of Nd isotopes via incongruent
39 weathering and Nd adsorption collectively modulate particulate ϵ_{Nd} through the length and duration of
40 river transport. An important implication of this study is that the ϵ_{Nd} offset between the leachates and
41 detrital phases of marine sediments can be a robust tracer for investigating continental weathering and
42 transport during glacial-interglacial periods.

43

44 **Keywords**

45 Basalt weathering; Rajmahal Volcanics; adsorption; incongruent behaviour of Neodymium isotopes,
46 riverine transport, water-particle interaction

47

48 **1. Introduction**

49 Radiogenic neodymium isotope composition ($^{143}\text{Nd}/^{144}\text{Nd}$, expressed as ϵ_{Nd} , Goldstein and Jacobsen,
50 1987) has wide applications in investigating crustal extraction and evolution, determining continental
51 weathering fluxes and sediment sources, and tracing ocean water masses. ^{143}Nd is a α -decay product of
52 ^{147}Sm ($t_{1/2} = 106$ Byr). Therefore, the ϵ_{Nd} value of an igneous or metaigneous rock is governed by its age
53 and Sm/Nd ratio whereas the composition of the primary source rocks regulates ϵ_{Nd} of a sedimentary or
54 metasedimentary rock. An implicit requirement for unbiased application of ϵ_{Nd} is the congruent behavior
55 of Nd isotopes during weathering, i.e., ϵ_{Nd} of the parent rock, dissolved phase (river water) and the
56 weathering product (sediments) should be identical. The underlying basis for congruent behaviour of Nd
57 isotopes is the knowledge that after its initial release during weathering, Nd is dominantly transported in
58 the solid phase(s) (Piepgras et al., 1979; Elderfield and Greaves, 1982; Goldstein et al., 1984).
59 Insignificant, yet quantifiable difference between ϵ_{Nd} of source rock and river water, and between river
60 water and suspended particulate matter (SPM) were alluded to by early investigations (Goldstein and
61 Jacobsen, 1987). However, several studies have clearly documented the difference between ϵ_{Nd} of parent
62 rocks and the weathered products (Martin et al., 1999; Ohlander et al., 2000; Aubert et al., 2001; Ma et
63 al., 2010; Babechuk et al., 2015; Banerjee and Chakrabarti, 2016; Horbe et al., 2022); between source
64 rocks and river/ground water (Andersson et al., 2001; Aubert et al., 2001; Negrel et al., 2001; Viers and
65 Wasserburg, 2004; Leybourne and Cousens, 2005; Wallrich et al., 2020); between river water and SPM
66 (Henry et al., 1996; Aubert et al., 2001; Rickli et al., 2013; Chatterjee and Singh, 2014; Merschel et al.,
67 2017; Hindshaw et al., 2018); between source rocks and SPM (Martin et al., 1999; Aubert et al., 2001);
68 and between leachable and detrital phases of sediments (Tricca et al., 1999; Adebayo et al., 2018; Sufke
69 et al., 2019; Jang et al., 2020; Larkin et al., 2021). These studies document incongruent behaviour of Nd

70 isotopes driven by incongruent weathering in catchments comprising of igneous, sedimentary, and
71 mixed lithologies. Therefore, incongruent behaviour of Nd isotopes during weathering is prevalent
72 across the globe, irrespective of the lithology of the catchment. The unraveling of the incongruent
73 behavior of Nd isotopes during weathering was possible due to advancement in instrumentation which
74 allowed for more precise ϵ_{Nd} determination, with uncertainties of up to ± 0.3 (Viers et al., 2008; Rousseau
75 et al., 2019; Moquet et al., 2020) compared to up to ± 0.9 in earlier studies (Goldstein and Jacobsen,
76 1987; Goldstein and Jacobsen, 1988).

77 Multiple mechanisms have been put forward for explaining the incongruent behaviour of Nd
78 isotopes. These include: (i) differential mineral weathering (Andersson et al., 2001; Aubert et al., 2001;
79 Ohlander et al., 2000; Viers and Wasserburg, 2004; Leybourne and Cousens, 2005; Chatterjee and Singh,
80 2014; Dausmann et al., 2019; Sufke et al., 2019; Wallrich et al., 2020); (ii) preferential release of more
81 labile phases of Nd (Goldstein and Jacobsen, 1987; Hindshaw et al., 2018; Jang et al., 2020; Horbe et al.,
82 2022); and (iii) disproportionate contributions from different lithologies to riverine SPM (Henry et al.,
83 1996; Chatterjee and Singh, 2014; Merschel et al., 2017) and surface sediments (Bouchez et al., 2011;
84 Garcon and Chauvel, 2014; Bayon et al., 2015; Bayon et al., 2020a). The incongruent behaviour and
85 release of radiogenic Nd isotopes discussed in this study could arise due to any one or a combination of
86 the processes mentioned above, and should not be misconstrued with Nd isotope fractionation.

87 Weathering profiles of granitic to granodioritic rocks, sedimentary rocks, and coal bearing units
88 unequivocally document incongruent behaviour of Nd isotopes (Aubert et al., 2001; Negrel et al., 2001;
89 Viers and Wasserburg, 2004; Ohlander et al., 2000; Wallrich et al., 2020; Horbe et al., 2022). During
90 basalt weathering, however, there is significant ambiguity on behaviour of Nd isotopes given that both
91 congruent (Martin et al., 1999; Nobre Silva et al., 2010) and incongruent (preferential release of

92 radiogenic Nd, Ma et al., 2010) release of Nd isotopes is reported. Additional data on Nd isotopes in
93 basaltic weathering profiles is required for a clear assessment of congruent vs. incongruent behaviour of
94 Nd isotopes during basalt weathering. In this study, this gap in knowledge is filled by quantifying the
95 trends and aberrations in Nd isotopes in the bulk rocks, weathered products and adsorbed
96 (oxyhydroxides) phases of two weathering profiles developed on basaltic rocks of the Rajmahal
97 Volcanics Province (RVP) in India (Supplementary Note SN1). Our study provides clear evidence of
98 incongruent behavior of Nd isotopes during weathering and capture of Nd isotope composition of
99 weathering solutions in the oxyhydroxide phases. Furthermore, utilizing the published data for fourteen
100 global rivers, we demonstrate that incongruent behaviour of Nd isotopes during weathering and
101 adsorption of dissolved Nd riverine transport influence the particulate ϵ_{Nd} composition at a global scale.

102 **2. Material and methods**

103 Two weathering profiles developed on the basaltic rocks of the RVP (Supplementary Note SN1)
104 were chosen after careful evaluation of their state of preservation and external contamination by aeolian
105 inputs (Supplementary Note SN2 and Fig SF3). Dried samples of basaltic parent rocks and their
106 weathered materials collected from the profiles were weighed in pre-cleaned quartz crucibles and
107 combusted at 550°C in a muffle furnace for ~5 hours to oxidize the organic matter. About 100 mg of
108 ashed samples and reference standards were accurately weighed in a pre-cleaned PFA vial (Savillex®).
109 To these vials, we added an acid mixture containing 3 mL of HCl and 1 mL of HNO₃ (both double-
110 distilled on PFA stills from concentrated analytical grade acids), and 2 mL of ultrapure concentrated HF.
111 The acid-sample mixture was quantitatively digested at 160°C for ~72 hours. The vials were opened
112 after they cooled to room temperature. All operation was conducted under clean workbench conditions
113 (Class-100) and the solutions were dried under identical environment. Subsequently, a few mL of HNO₃

114 was added to the residue for dissolution, followed by evaporation to drive-off residuary HF. The
115 digested samples were redissolved in ~60 g of 5% HNO₃. These solutions were analyzed by ICPMS.
116 The procedural blanks and sample replicates were processed in every batch of digestion. The HNO₃ and
117 HCl used for sample processing were double-distilled (DD) in a Savillex[®] DST-1000 sub-boiling
118 distillation system and the ultrapure grade HF was commercially procured.

119 For measurements on X-Ray spectrometer (XRF), fusion beads were made. In brief, the
120 powdered samples were accurately weighed and mixed with a flux of 65% lithium tetraborate and 35%
121 lithium metaborate in a 1:10 ratio. After thorough mixing, a few grains of lithium bromide were added to
122 the mixture. These mixtures were quantitatively transferred into platinum crucibles and melted at 1250
123 °C. The melted mixtures were poured into pre-heated platinum moulds to form the fusion beads of
124 required shape and size.

125 Selective extraction of the exchangeable and amorphous Fe-Mn oxyhydroxides phases was
126 carried out by a two-step leaching procedure (Gupta and Chen, 1975; Chen et al., 2012). For
127 exchangeable fractions, ~ 3 g of powdered sample was added to a pre-cleaned 50 mL centrifuge tube and
128 leached with 40 mL of 1N ammonium acetate (Sigma Aldrich, > 99.99% purity) buffered at pH 7 with
129 superpure ammonium hydroxide. These mixtures were kept overnight on a reciprocating shaker at 400
130 rpm and finally centrifuged at 5000 rpm. The supernatant fractions were decanted into precleaned PFA
131 beakers. The residues were washed three times with Milli-Q water (18.2 MΩ) and washings were
132 collected and mixed with the supernatant. These solutions were dried and redissolved in 5% HNO₃ for
133 elemental analysis and another aliquot in 2N HCl for chromatographic purification required for Nd
134 isotopic analysis. To extract the oxyhydroxides phases, a mixture of 40 mL 0.005 N hydroxylamine
135 hydrochloride (HH; 99.999% purity), 1.5% acetic acid (≥99.99% purity) and 0.03 N

136 ethylenediaminetetraacetic acid (EDTA; 99.995% purity), buffered to pH 4 with sodium hydroxide, was
137 added to the residues left after extraction of exchangeable phase. These sample-reagent mixtures were
138 kept for one hour on a reciprocating shaker at 400 rpm. Thereafter, the procedure followed was the same
139 as outlined above for extraction of exchangeable fractions.

140 **2.1. Analysis of major and trace element composition**

141 The fusion beads were analyzed to measure the major element concentrations using a Bruker[®] Tiger
142 S-8 WD-X-Ray Spectrometer. The accuracy of the measurements was evaluated by analysis of certified
143 reference standards NIST 2711A (Montana II Soil), SDC-1 (Mica Schist) and MESS-3 (Marine
144 Sediment). The measurement accuracies were better than $\pm 8\%$. The analytical reproducibility, based on
145 replicate analyses of the same sample, was within $\pm 5\%$.

146 Trace element concentrations were measured by a QQQ-ICP-MS (Agilent[®] 8900 at IISc, Bangalore)
147 following multi-element external calibration and internal standard addition. Certified reference standards
148 BCR-2 (Columbia River Basalt), BHVO-2 (Hawaiian Basalt) and GSP-2 (Granodiorite) were analyzed
149 to determine the measurement accuracy, which was 5% or better for La, Sm, Th, Sc and Nb and better
150 than 9% for Nd. The analytical reproducibility, evaluated by replicate analyses, was within $\pm 2\%$ for
151 trace elements.

152 The major and trace element concentrations in the exchangeable and oxyhydroxide fractions were
153 measured by a quadrupole ICP-MS (ThermoScientific[®] X Series 2) at IISER Kolkata. Based on the
154 analysis of certified reference standard BHVO-2 and NIST-traceable standards IV-Stock 26 and IV-
155 Stock 8 (Inorganic Ventures[®]), the measurement accuracy was better than 3% for Mn and 10% for Nd.

156 Based on replicate analyses, analytical reproducibility of Mn and Nd are within $\pm 7\%$ for exchangeable
157 and oxyhydroxide phases.

158 **2.2. Purification of Nd and measurement of Nd isotope composition**

159

160 **2.2.1. Bulk samples of weathering profiles**

161 Nd separation from the samples followed a modified method of Lei et al. (2019). The REEs were
162 separated in a two-step cation exchange column chromatography. The first column was loaded with 0.8
163 mL of AG50W-X8 resin, washed with 6N HCl, 3N HNO₃ and Milli-Q and pre conditioned with 2N
164 HCl. The sample solution was loaded in 2N HCl medium and was eluted with 2N HCl and 2.5N HNO₃
165 to remove the major elements. The REE fractions were collected in 7N HNO₃, dried and redissolved in
166 0.15N HCl. The second column was loaded with 1 mL of Ln Spec resin, washed with 6N HCl and Milli-
167 Q and preconditioned with 0.15N HCl. The separated REE fractions from the first column were dried
168 down and then loaded in 0.15N HCl medium and eluted with 0.15N HCl to remove Ba. The Nd fractions
169 were collected in 0.25N HCl and the column was eluted with 6N HCl to remove Sm. The Nd isotope
170 measurements were carried out by a MC-ICP-MS (ThermoScientific® Neptune Plus) facility at IISER
171 Kolkata. Mass bias correction was done by normalizing the measured ¹⁴³Nd/¹⁴⁴Nd ratios with a
172 ¹⁴⁶Nd/¹⁴⁴Nd ratio of 0.7219. Analysis of the USGS standard BCR-2 yielded a ¹⁴³Nd/¹⁴⁴Nd ratio =
173 0.512630 \pm 0.000002 (2 σ , n=2), which agreed well with the reported value of 0.512637 \pm 000017 (Weis et
174 al., 2006). The mean external reproducibility of the measured ¹⁴³Nd/¹⁴⁴Nd ratio evaluated by replicate
175 sample analyses is \pm 0.000009 (2 σ , n=4).

176 **2.2.2. Oxyhydroxide phases**

177 The Nd concentrations in the oxyhydroxides phases ([Nd]_{oxy}) were significantly higher than those in
178 the exchangeable phases ([Nd]_{exch}), with [Nd]_{oxy}/[Nd]_{exch} ratios (Supplementary Table ST3) as high as 18

179 in the Dalahi profile (mean: 8) and 63 in Pakuria profile (mean: 18). Such results clearly indicate that the
180 oxyhydroxides phases are the dominant carrier of adsorbed Nd. Therefore, Nd separation and Nd isotope
181 measurements were carried out only for the oxyhydroxide phases. Our observation of oxyhydroxide
182 phases as the dominant carrier of the adsorbed Nd is in line with the published results (Adebayo et al.,
183 2018; Larkin et al., 2021).

184 The REEs were separated using a column calibration that is slightly different than that described
185 above for the bulk phases. The columns were loaded with ~2 mL of AG50W-X8 resin, washed with 6N
186 HCl and Milli-Q and conditioned with 2N HCl. The sample solution was loaded in 2N HCl on the
187 preconditioned column and was washed with 2N HCl and 6N HCl. The REE fractions were eluted in 6N
188 HCl. Hereafter, the purification of Nd from REE fractions followed the procedure as outlined above for
189 the bulk phases. The Nd isotope measurements were carried out by a MC-ICP-MS (ThermoScientific®
190 Neptune Plus) facility at the Physical Research Laboratory (PRL), Ahmedabad. Mass bias correction
191 followed a normalization scheme with a $^{146}\text{Nd}/^{144}\text{Nd}$ ratio of 0.7219. The standard JNdi-1 was measured
192 to evaluate the instrumental stability and yielded an average value of $^{143}\text{Nd}/^{144}\text{Nd} = 0.512114 \pm 0.000017$
193 (2σ , n=11), consistent with the published value of $^{143}\text{Nd}/^{144}\text{Nd} = 0.512115 \pm 0.000007$ (Tanaka et al.,
194 2000). Measured $^{143}\text{Nd}/^{144}\text{Nd}$ ratios for the reference standards were, 0.512637 ± 0.000013 (2σ , n=3) for
195 BCR-2 and 0.512984 ± 0.000015 (2σ , n=7) for BHVO-2, which were in agreement with the reported
196 values of 0.512637 ± 0.000017 and 0.512987 ± 0.000010 , respectively (Weis et al., 2006). Analysis of four
197 procedural replicate samples provides the mean external reproducibility of the measured $^{143}\text{Nd}/^{144}\text{Nd}$
198 ratio to be ± 0.000005 (2σ , n=4).

199 **3. Results and discussion**

200 **3.1. Incongruent behaviour of radiogenic Nd during chemical weathering**

201 The chronology of the RVP basalts is well constrained (118 ± 2 Myr, Baksi, 2022). Prior to isotopic
202 analysis of the weathering profiles, their state of preservation was verified based on elemental
203 composition (Supplementary Note SN2). The compositions of these profiles (Supplementary Table ST1)
204 demonstrate progressive chemical weathering, as evident from drop in [Na], [Ca], [Mg], Si/Al, and
205 increase of [Al] and chemical index of alteration (CIA) towards the surface (Fig. 1). The Nd/Al, Mn/Al
206 and Fe/Al demonstrate upward increasing trends (Fig. 1), suggestive of Nd adsorption onto the
207 secondary phases, specifically the Fe-Mn oxyhydroxides. The incongruent release of radiogenic Nd is
208 unequivocal and can be observed in the upwardly decreasing trend of ϵ_{Nd} (Fig. 1) and a strong inverse
209 correlation between CIA and ϵ_{Nd} (Fig. 2a). These observations, together with the significant inverse
210 correlation of Sm/Nd ratio with CIA (Fig. 2b), underscore preferential weathering of minerals that have
211 higher Sm/Nd (Aubert et al., 2001; Negrel, 2006; Garzanti et al., 2011; Garcon et al., 2014; Dausmann
212 et al., 2019) and a more radiogenic ϵ_{Nd} composition compared to the parent rock (host basalt).
213 Preferential weathering of pyroxenes relative to feldspars was inferred from the composition of rivers
214 draining these RVP basalts in the study area (Kisku et al., 2020). Our inference of preferential
215 weathering of minerals with higher Sm/Nd ratio is consistent with multiple published works on basalt
216 weathering (Martin et al., 1999; Ma et al., 2010; Liu et al., 2013; Babechuk et al., 2014).

217 The fraction of Nd released from parent basalts during weathering was quantified by normalizing
218 its concentrations with the immobile element Th, which is used to correct for variation in Nd abundance
219 due to mass loss and/or addition. This approach (Supplementary Note SN3) indicates that up to 40 % Nd
220 is lost from the parent basalts during chemical weathering. The ϵ_{Nd} of the residual phases post weathering
221 was quantified by mass balance considerations of the [Nd] and ϵ_{Nd} signatures of bulk materials and

222 adsorbed (oxyhydroxide) phases (see [Supplementary Note SN4](#), [Supplementary Table ST3](#)). We observe
223 that the ϵ_{Nd} values of the residual phases are lower by up to 0.94 units compared to the bulk materials.
224 Furthermore, the ϵ_{Nd} values of the bulk materials in the weathering profiles are primarily modulated by
225 the residual phases since they account for a major fraction of Nd (74 % to 98 %, [Supplementary Table](#)
226 [ST3](#)).

227 A measure of radiogenic Nd released to the weathering solutions can be assessed from the
228 differences of ϵ_{Nd} between the parent rock and residual phases ($\Delta\epsilon_{Nd}^{P-Res}$). The $\Delta\epsilon_{Nd}^{P-Res}$ is characterized by a
229 downward decreasing trend and exhibits a strong positive correlation with CIA ([Fig. 3](#), [Supplementary](#)
230 [Table ST3](#)). This indicates that the degree of release of radiogenic Nd to the weathering fluid scales with
231 degree of chemical weathering. The importance of solid-solution interaction of major cations in river
232 catchments has been previously recognized (Clow and Mast, 2010; Tipper et al., 2021) It has been
233 widely reported that Nd is highly susceptible to water-particle interactions, whereby dissolved Nd is
234 adsorbed onto the solid phases, specifically the Fe-Mn oxyhydroxides (Fee et al., 1992; Steinmann and
235 Stille, 2008; Ma et al., 2007; Liu et al., 2019; Bai et al., 2023). In both the weathering profiles we
236 observe a strong positive correlation between $\Delta\epsilon_{Nd}^{P-Res}$ vs. $\frac{[Mn]_{ox}}{[Mn]_{bulk}}$ ([Fig. 4](#)), where ox and bulk refer to the
237 oxyhydroxide (chemically extracted) and bulk phases, respectively. This observation supports the
238 hypothesis that the Mn oxyhydroxide phases faithfully record the Nd isotope signature (ϵ_{Nd}) of the
239 weathering solution via adsorption. The present observation of Mn oxyhydroxides being the dominant
240 adsorbent of Nd isotopes from the weathering solution is consistent with the earlier reports that
241 oxyhydroxides are a major carrier of LREEs in the weathering profiles developed on basaltic substrates
242 (Ma et al., 2007; Bai et al., 2023). Our results and published body of work (Larkin et al., 2021; Bayon et

243 al., 2020b) lend support to the idea that ϵ_{Nd} of Fe-Mn oxyhydroxide phases can be used as a proxy for
244 hydrogenous ϵ_{Nd} in freshwater environments.

245 **3.2. A hypothesis for modulation of particulate ϵ_{Nd} via river transport at a global scale**

246 Many studies have documented pervasive adsorption of dissolved Nd onto the SPM during riverine
247 transport (Elderfield et al., 1990; Sholkovitz, 1995; Shiller, 2002; Steinmann and Stille, 2008; Smith and
248 Liu, 2018). In aquatic systems, the LREEs are preferentially removed from dissolved phase onto Fe-Mn
249 oxyhydroxides (Elderfield et al., 1990; Fee et al., 1992; Sholkovitz, 1995; Shiller, 2002; Steinmann and
250 Stille, 2008; Liu et al., 2019). In addition, organic colloids play a significant role in transporting the
251 REEs and facilitating their removal from solution (Land et al., 1999; Ingri et al., 2000; Dang et al.,
252 2023).

253 We contend that adsorption of dissolved Nd in rivers is globally significant because the residence
254 time of water and SPM in river catchments, varying from a few days to years (Wallbrink et al., 1998;
255 Ciffroy et al., 2003; McGuire and McDonnell, 2006; Sprenger et al., 2019), are orders of magnitude
256 higher than the experimentally determined kinetics of adsorption of REEs in aqueous medium
257 (Davranche et al., 2005; Ashour et al., 2017; Mosai et al., 2019; Briao et al., 2021). Furthermore,
258 significant abundances of adsorbents, particularly the clay minerals and Fe-Mn oxyhydroxides, in the
259 riverine SPM (Land et al., 1999; Ingri et al., 2000; Steinmann and Stille, 2008) provide the sites for
260 adsorption of dissolved Nd.

261 In addition to ubiquitous and unequivocal reports of adsorption of dissolved Nd in rivers,
262 majority of studies, including ours, document preferential release of radiogenic Nd via incongruent
263 chemical weathering (Aubert et al., 2001; Negrel et al., 2001; Viers and Wasserburg, 2004; Ma et al.,

264 2010; Dausmann et al., 2019). This is consistent with dissolved Nd being more radiogenic (higher ϵ_{Nd})
265 than the SPM or the source rocks (Henry et al., 1996; Aubert et al., 2001; Rickli et al., 2013; Chatterjee
266 and Singh, 2014; Merschel et al., 2017; Hindshaw et al., 2018). Higher ϵ_{Nd} is also observed in SPM
267 bound leachable phases compared to the residual/detrital phases in rivers (Tricca et al., 1999; Adebayo et
268 al., 2018; Larkin et al., 2021), fjords (Jang et al., 2020), lakes (Sufke et al., 2019), and oceans
269 (Tachikawa et al., 2004; Chen et al., 2012; Wilson et al., 2013). Preferential weathering of easily
270 weatherable (less weathering resistant) phases, which are characterized by higher Sm/Nd and therefore
271 elevated ϵ_{Nd} than their host/bulk rocks, has been put forward as a plausible explanation (Aubert et al.,
272 2001; Garzanti et al., 2011; Chatterjee and Singh, 2014; Garcon et al., 2014; Dausmann et al., 2019) for
273 more radiogenic Nd in the leachable phases. However, a few studies also indicate preferential release of
274 unradiogenic Nd over its radiogenic counterpart during weathering (Andersson et al., 2001; Ohlander et
275 al., 2000), which results in dissolved Nd to be less radiogenic than the source rock(s) or SPM (Goldstein
276 and Jacobsen, 1987; Spencer et al., 1995; Andersson et al., 2001). The preferential supply of
277 unradiogenic Nd can either result from its incongruent release during weathering of the source rocks or
278 due to external inputs. It is noteworthy that the explanations put forward by studies documenting
279 enrichment of unradiogenic Nd in the fluid phase do not always indicate its preferential release. For
280 instance, the sole study that suggested preferential loss of unradiogenic Nd during weathering (Ohlander
281 et al., 2000), also recognized the involvement of external sources, namely the impact of dust borne Nd
282 supply. Therefore, the evidence in favour of preferential release of unradiogenic Nd via incongruent
283 weathering remains tenuous.

284 The growing body of studies, including this one, documenting incongruent behaviour of Nd
285 isotopes together with ubiquitous evidence of Nd adsorption in rivers lead us to posit that the particulate

286 ϵ_{Nd} would be modulated via solid-solution interaction during riverine transport. We hypothesise that the
287 degree of Nd adsorption is dominantly a function of water-particle interaction time in the catchment area
288 and the streams, which is primarily regulated by water discharge (Anderson et al., 1997; Land et al.,
289 1999; Hindshaw et al., 2019; Liu-Lu et al., 2022). Published studies clearly document the water-particle
290 contact time as an important driver of adsorption of elements and metals in aquatic systems of streams
291 and rivers (Worman, 1998; Worman et al., 1998; Hindshaw et al., 2019; Liu-Lu et al., 2022). Thus, we
292 posit that particulate ϵ_{Nd} would be sensitive to riverine discharge (Q) if the ϵ_{Nd} values of the dissolved
293 and SPM phases are different. A higher degree of Nd adsorption during the low flow period (LQ),
294 relative to the high flow period (HQ), would result in positive values of $\Delta\epsilon_{Nd}^{LQ-HQ}$ in the SPM if the waters
295 have a higher ϵ_{Nd} value than the SPM. On the contrary, negative values of $\Delta\epsilon_{Nd}^{LQ-HQ}$ would result from the
296 SPM having more radiogenic Nd than the waters. In case of insignificant ϵ_{Nd} difference between the river
297 water and SPM, the $\Delta\epsilon_{Nd}^{LQ-HQ}$ values would be indistinguishable from zero.

298 **3.3. Discharge dependency of river particulate ϵ_{Nd}**

299 We re-evaluated available discharge and particulate ϵ_{Nd} data of fourteen rivers covering a
300 latitudinal extent of 40° S to 40° N. They are Uruguay, Parana and Changjiang in the low- to mid-
301 latitudes, Ganga, Brahmaputra and Minjiang in the low latitudes, and Amazon, Orinoco, Maroni,
302 Solimoes, Madeira, Tumbes, Xingu and Tapajos in the tropics. The river lengths range from 230 km
303 (Tumbes River) to 6400 km (Amazon River) and the basin areas vary from 5×10^3 km² (Tumbes River)
304 to 6×10^6 km² (Amazon River). The annual discharges of these rivers vary over four orders of magnitude,
305 from 4 km³ to 6300 km³. Together these rivers contribute ~43% of the global river water flux (Palmer
306 and Edmond, 1993; Henry et al., 1996; Dai et al., 2002; Viers et al., 2008; Do et al., 2020; Jian et al.,

307 2020b; Moquet et al., 2020). The drainage basins are characterized by basaltic (Uruguay), sedimentary
308 (Parana), and mixed lithologies (the rest).

309 To elucidate the impact of solid-solution interaction time, nine sets of time-series particulate ϵ_{Nd}
310 data of eight rivers were first evaluated (Supplementary Table ST4). This approach is based on the
311 knowledge that water discharge influences the residence time of water in river catchments over seasonal
312 and annual timescales (Manaka et al., 2017; Hindshaw et al., 2019; Liu-Lu et al., 2022; Zhang et al.,
313 2022). Therefore, timeseries data of riverine particulate ϵ_{Nd} can provide insight into duration of solid-
314 solution interaction and its impact on particulate ϵ_{Nd} . In addition, catchment scale time-series data limits
315 the impact of variable source rock composition and topography of a river basin, at least for smaller
316 catchments. We argue that if the ϵ_{Nd} of river water is higher than their conjugate SPM, then the ϵ_{Nd} of the
317 SPM will have a discharge dependent signature, with low-discharge periods characterised by higher
318 particulate ϵ_{Nd} . Therefore, for our hypothesis to be valid, an inverse relationship between Q and
319 particulate ϵ_{Nd} should be observed in each individual river catchment.

320 There are indeed significant ϵ_{Nd} -Q inverse relationships observed individually for each of the
321 eight in nine sets of time-series particulate ϵ_{Nd} data (Supplementary Table ST5, Fig. 5). In addition, out
322 of discrete seasonal data available for eight rivers, inverse ϵ_{Nd} -Q variation trends are observed for each
323 of the six rivers (see Supplementary Note SN5 for more details on river data). A global ϵ_{Nd} -Q inverse
324 relationship for the combined time-series data of all the rivers is neither observed nor anticipated given
325 that the SPM are derived from lithologies that are characterized by distinctly different ϵ_{Nd} values. Our
326 hypothesis dictates that the ϵ_{Nd} values of sediments, once generated via weathering of the source rocks in
327 a river catchment, would be modulated during transport by responding to variable water discharge as

328 explained above. To calculate the mean particulate ϵ_{Nd} of a flow regime, the time-series data were
329 appropriately averaged after excluding the outliers resulting from unusual fluctuations (see
330 [Supplementary Note SN6, Supplementary Table ST4](#)). As predicted, the mean ϵ_{Nd} values during lean
331 flow periods are higher than high flow periods, with $\Delta\epsilon_{Nd}^{LQ-HQ}$ varying in the range of 0.30 to 2.94 units.
332 Similarly, the discrete seasonal data for six rivers demonstrate that the particulate ϵ_{Nd} values are more
333 radiogenic, by up to 2.52 units, during low flow periods compared to high flow conditions
334 ([Supplementary Table ST4](#)). Therefore, observations based on both time-series and discrete seasonal
335 data reinforce our hypothesis that the particulate ϵ_{Nd} values are modulated by Nd adsorption during
336 riverine transport. In addition, the ϵ_{Nd} -Q relationship of the rivers provides support to the idea that rivers
337 waters have higher ϵ_{Nd} than their conjugate SPM, consistent with existing studies on rivers (Henry et al.,
338 1996; Aubert et al., 2001; Rickli et al., 2013; Chatterjee and Singh, 2014; Merschel et al., 2017;
339 Hindshaw et al., 2018).

340 **3.4. Importance of water-particle interaction time**

341 The global particulate ϵ_{Nd} -Q relationship ([Fig. 5](#)), is consistent with laboratory studies (Harvey et
342 al., 1996; Worman, 1998), field investigations (Worman et al., 1998; Manaka et al., 2017; Hindshaw et
343 al., 2019; Liu-Lu et al., 2022; Zhang et al., 2022) and modelling (Worman, 1998; Worman et al., 1998)
344 that document the fluid-particle interaction time as a dominant parameter in the adsorption of dissolved
345 elements in freshwater systems. Studies based on natural and synthetic adsorbent materials report the
346 metal adsorption kinetics to be fast, ranging from a few minutes to a few days (Davranche et al., 2005;
347 Ashour et al., 2017; Mosai et al., 2019; Briao et al., 2021) for reaching equilibrium concentrations in the
348 solid phase. Unfortunately, studies on timescale of metal transport in natural environment of streams and

349 rivers are rather sparse. Limited bodies of work, based on a ^{51}Cr tracer, indicate that the transport
350 timescales of metals are much longer than what the laboratory experiments suggest (Worman, 1998;
351 Worman et al., 1998; Johansson et al., 2001). Notably, these studies show that the removal timescales of
352 reactive metals in natural waters vary as a function of water-particle interaction time and the length of
353 transport.

354 The $\epsilon_{\text{Nd}}-Q$ relationship holds good for a set of global rivers (Fig. 5) characterised by discharges
355 that vary by five orders of magnitude and river lengths as high as a few thousand kilometres. Such an
356 observation implies that adsorption reactions take longer time to reach equilibrium in rivers than in the
357 laboratory experiments, consistent with inferences drawn from studies on metal transport in rivers
358 (Worman, 1998; Worman et al., 1998; Johansson et al., 2001). The slower kinetics of Nd adsorption in
359 rivers, as implied from $\epsilon_{\text{Nd}}-Q$ relationship (Fig. 5), could be a result of one or a combination of the
360 following reasons: (i) the stability of rare earth complexes with carbonate ions and organic ligands is pH
361 dependent and therefore, the adsorption of REE would be limited particularly at elevated pH (Goldstein
362 and Jacobsen, 1987; Adebayo et al., 2018), (ii) the mass of adsorbent materials such as Fe-Mn
363 oxyhydroxides per unit volume of water (dose rate) are significantly lower in the rivers than those used
364 in laboratory studies, (iii) the stability of Fe-Mn oxyhydroxides may respond to local changes in redox
365 state via processes such as organic matter metabolization (Aucour et al., 2003; Neidhardt et al., 2014)
366 which would adversely impact Nd adsorption if the adsorbent material(s) become thermodynamically
367 unstable during transport. (iv) the presence of materials such as quartz in the river SPM reduces the
368 adsorption potential of SPM. Available studies indicate that cases of slow adsorption kinetics are better
369 explained by the nature of adsorbent materials rather than simple kinetic mechanisms (Ashour et al.,
370 2017; Mosai et al., 2019).

371 The indisputable support for the idea that the difference of water-particle interaction times
372 between the flow regimes exerts a dominant influence on the particulate ϵ_{Nd} via adsorption of dissolved
373 Nd comes from the observation that the differences of ϵ_{Nd} values between the lean and peak flow periods
374 ($\Delta\epsilon_{Nd}^{LQ-HQ}$) scale with the magnitude of discharge contrast (Q_c) between these periods (Fig. 6).
375 Furthermore, the discrete seasonal data (Fig. 6) for six rivers e also support the above inference drawn
376 based on the time-series data and therefore support our interpretative framework. However, we advocate
377 caution about the pitfalls associated with unusual fluctuations in the discrete seasonal data that may bias
378 the estimates of ϵ_{Nd}^{LQ} and ϵ_{Nd}^{HQ} values. Mass dependent Nd isotope fractionation, although reported for Nd
379 adsorption onto oxyhydroxide phases such as goethite, does not bias the radiogenic isotope composition,
380 i.e. the ϵ_{Nd} values (Bai et al., 2023). It is intuitive to reason that the $\Delta\epsilon_{Nd}^{LQ-HQ}$ values are unlikely to be
381 impacted as the effect of isotope fractionation, if any, and would be nearly cancelled out while
382 computing the seasonal ϵ_{Nd} difference. Thus, the effect of mass-dependent fractionation for $\Delta\epsilon_{Nd}^{LQ-HQ}$ is
383 excluded in subsequent discussions.

384 The signature of seasonal variation of adsorption of dissolved Nd would be best captured in the
385 particulate ϵ_{Nd} rather than in the [Nd] or Nd/Al ratios because one or a combination of the following
386 reasons: (i) the Nd concentrations are measured with a precision of a few percent at best. Therefore,
387 adsorption accounting for up to a few percent Nd in the SPM may not be clearly discernible, whereas the
388 associated changes in ϵ_{Nd} is easily detected due to the higher precision of isotopic measurements; (ii)
389 given that adsorption of Nd is influenced by the abundance of secondary phases such as clay minerals
390 and Fe-Mn oxyhydroxides, the change in concentrations of Nd will be in the same direction as that of
391 Al, Fe or Mn. Therefore, the change in the ratios (Nd/Al, Fe/Al or Mn/Al) in response to Nd adsorption

392 would be harder to distinguish between periods of low and high flow conditions; (iii) the modulation of
393 particulate ϵ_{Nd} via adsorption of dissolved Nd would be a function of ϵ_{Nd} differences between the river
394 water and the SPM ($\Delta\epsilon_{Nd}^{Riv-SPM}$), in addition to the degree of Nd adsorption. Therefore, the change in
395 particulate ϵ_{Nd} would be higher and easily detectable even for a small quantity of Nd adsorbed, provided
396 the $\Delta\epsilon_{Nd}^{Riv-SPM}$ is considerable. Lack of combined data on [Nd] and ϵ_{Nd} in the river water, SPM and
397 adsorbed phases does not allow us to quantitatively evaluate the quantitative impact of ($\Delta\epsilon_{Nd}^{Riv-SPM}$) vis-à-
398 vis degree of Nd adsorption on the particulate ϵ_{Nd} . Nevertheless, we demonstrate the coupled impact of
399 these two driving parameters on the particulate $\Delta\epsilon_{Nd}$ (see [Supplementary Note SN7](#)) through a simple
400 mass-balance model. For example, a $\Delta\epsilon_{Nd}^{LQ-HQ}$ value of 1 can be achieved at ~6-10% difference of Nd
401 adsorption between the flow regimes (Δf_{Nd}^{LQ-HQ}) if $\Delta\epsilon_{Nd}^{Riv-SPM}$ values are in the range of 10-15. However, it
402 would require a value of ~20% Δf_{Nd}^{LQ-HQ} to meet the same $\Delta\epsilon_{Nd}^{LQ-HQ}$ if $\Delta\epsilon_{Nd}^{Riv-SPM}$ is decreased to 5
403 ([Supplementary Fig. SF4](#)).

404 The degree of Nd adsorption and its impact on particulate ϵ_{Nd} would depend on, in addition to
405 solid-solution contact time, a number of other factors such as: solution pH, abundance and stability of
406 adsorbents such as Fe-Mn oxyhydroxides, the $\Delta\epsilon_{Nd}$ between SPM and water, and the initial [Nd] of SPM
407 before initiation of adsorption. Despite such complexities, our evaluation and interpretative framework
408 of riverine transport driven modulation of particulate ϵ_{Nd} is supported by the data of rivers that account
409 for ~43 % of the global water flux and cover wide lithological, geographical and climate variation.
410 Therefore, existing data support the proposition that the transport timescale exerts a dominant control on
411 the riverine particulate ϵ_{Nd} values on a global scale.

412 **3.5. Role of SPM load and its characteristics**

413 A closer inspection of the discharge and SPM data reveals that the water residence times in the
414 catchments exert an indirect control on Nd adsorption by impacting the quantity and the nature (physical
415 and chemical properties) of the SPM. Compared to the low flow periods, the peak flow periods usually
416 have higher SPM concentrations and lower CIA values (Supplementary Fig. SF5). In addition, with the
417 exception of the Changjiang River data, particulate Fe/Al and Mn/Al ratios show inverse correlations
418 with the SPM concentrations (Supplementary Fig. SF6). These observations together indicate that
419 formation of secondary phases, particularly the Fe-Mn oxyhydroxides, is favoured more during the dry
420 periods due to higher water residence time (Ingri and Widerland, 1994; Land et al., 1999; Smith and Liu,
421 2018). As a consequence, Nd adsorption is favourably impacted in the lean periods due to both longer
422 water-particle contact time and higher proportions of adsorbent phases. This idea draws further support
423 from available time-series data in terms of inverse correlations of Nd/Al ratios with the SPM
424 concentrations (Supplementary Fig. SF7), Mn/Al, and Fe/Al ratios barring the Madeira River data
425 (Supplementary Fig. SF8). The weak to moderately strong correlations shown in supplementary figures
426 SF5 – SF8 should not be viewed to undermine our interpretation that the physical and chemical
427 characteristics of the SPM influence Nd adsorption. This is because the distributions of Nd in the river
428 water and the SPM are also regulated by organic complexes, the importance of which has not assessed in
429 this study.

430 **3.6. Impact of length and duration of river transport on particulate ϵ_{Nd}**

431 The cumulative water-particle contact time in rivers is a function of both the residence time of
432 water (regulated by water discharge) as well as length over which the transport takes place. Available
433 studies document importance of both these factors in regulating the solid-solution interaction processes
434 during stream transport (Worman, 1998; Johansson et al., 2001; Hindshaw et al., 2019; Liu et al., 2019;

435 Liu-Lu et al., 2022). The influence of transport length on particulate ϵ_{Nd} is clearly evident in the plot of
436 $\Delta\epsilon_{Nd}^{LQ-HQ}$ vs. the length of the rivers (Fig. 7). A strong negative correlation is supportive of the idea that as
437 the degree of Nd adsorption increases and approaches closer to equilibrium due to longer transport, the
438 $\Delta\epsilon_{Nd}^{LQ-HQ}$ decreases. Therefore, the relationships of $\Delta\epsilon_{Nd}^{LQ-HQ}$ with discharge contrast (Fig. 6) and river length
439 (Fig. 7) demonstrate the combined influence of both the length and duration of riverine transport on the
440 seasonal difference of the particulate ϵ_{Nd} . If differential inputs from lithologies and their mixing were
441 important, the $\Delta\epsilon_{Nd}^{LQ-HQ}$ values would have been higher for large rivers owing to more diverse lithologies
442 expected in larger basins. However, the observed inverse correlation (Fig. 7), in contrast, lends credence
443 to our contention that the impact of variable inputs from lithologies on seasonal particulate ϵ_{Nd} data is far
444 less significant compared to the duration and length of riverine transport.

445 3.7. Evaluation of alternative mechanisms

446 The observed particulate ϵ_{Nd} -Q relationship (Fig. 5) needs to be evaluated for alternative
447 causative mechanisms. Firstly, the flow regimes may cause preferential erosion and weathering of
448 specific lithology due to differential flow paths (Ibarra et al., 2016; Zhong et al., 2017). Therefore,
449 discharge variation can result in variable particulate ϵ_{Nd} due to differential lithological inputs between
450 flow regimes, at least in catchments with mixed lithologies. Additionally, river transport can cause
451 hydrodynamic size sorting of particulate matter and different size fractions can be sourced from different
452 lithologies (Bouchez et al., 2011; Garcon and Chauvel, 2014; Bayon et al., 2020a). For example, basaltic
453 particles have been suggested to be preferentially transported with the finer size fractions in the riverine
454 SPM (Garcon and Chauvel, 2014; Bayon et al., 2020a). Therefore, the observed particulate ϵ_{Nd} -Q trend
455 can be caused, at least partially, due to variable mixing of SPM derived from different lithologies or

456 size/mineral fractions. This notion of mixing, however, is not supported as none of the time-series data
457 of rivers considered in this study defines a mixing trend in the $\epsilon_{\text{Nd}} - [\text{Nd}]^{-1}$ space (Supplementary Fig.
458 SF9). Rousseau et al. 2019, based on trace element composition, invoked mixing of basic and granitic
459 rocks to explain the observed time-series ϵ_{Nd} variation in the Maroni River SPM. However, the $\epsilon_{\text{Nd}} - [\text{Nd}]^{-1}$
460 plot for the Maroni River SPM data does not indicate mixing between two end-members
461 (Supplementary Fig. SF9). While we recognize that time-series data may be partly influenced by mixing
462 of sources in specific catchments, we contend that drastic variation of mixing proportions over seasonal
463 time scales are unlikely to be significant and thus, cannot be the primary cause for the observed $\epsilon_{\text{Nd}} - Q$
464 relationship at a global scale. Secondly, fractionation of REEs is a function of age and differentiated
465 nature of the mantle from which the rocks are derived. Given that the younger rocks produced via
466 mantle melting will be characterized by higher Sm/Nd ratios, the particulate ϵ_{Nd} can also be influenced
467 by the source rock ages (Goldstein and Jacobsen, 1988; Tricca et al., 1999; Peucker-Ehrenbrink et al.,
468 2010). The effect of source rock age and composition on the particulate ϵ_{Nd} would be best reflected
469 through an inverse correlation between the depleted mantle model age (T_{DM}) and the $^{147}\text{Sm}/^{144}\text{Nd}$ ratio
470 (Goldstein and Jacobsen, 1988; Tricca et al., 1999). In contradiction to this expectation, these two
471 parameters define significant positive correlations for each of all the rivers (Fig. 8), thus clearly
472 indicating that the particulate Sm/Nd ratios and ϵ_{Nd} are more likely controlled by processes of weathering
473 and transport than by the variation in the source rock age and composition. Such an observation further
474 lends credence to our contention that the nature and variability of the source rock compositions play
475 insignificant role in impacting the observed particulate $\epsilon_{\text{Nd}} - Q$ variation trends in the time-series and
476 seasonal data, although the source rocks would be important in driving the initial ϵ_{Nd} value of the
477 sediments generated after weathering in a catchment. More notably, our observations (Fig. 8) caution

478 against using Nd isotope model ages of the riverine SPM without an appropriate evaluation of the
479 impact of weathering and transport on the Sm/Nd ratio and ϵ_{Nd} of the riverine particulate matter.

480 **4. Utility of ϵ_{Nd} difference between leachate and detrital phases as a tracer of** 481 **glacial-interglacial weathering**

482 Our re-evaluation of published ϵ_{Nd} data of global rivers indicate that the discharge periods
483 characterized by a large $\Delta\epsilon_{Nd}^{Riv-SPM}$ or higher Nd adsorption or a combination of both would result in an
484 increased difference in ϵ_{Nd} between the leachate and residual (detrital) phase of marine sediments
485 ($\Delta\epsilon_{Nd}^{Leach-Res}$). The temporal variation of $\Delta\epsilon_{Nd}^{Leach-Res}$ in the glacial-interglacial weathering records from
486 fjords and marine sedimentary archive has been primarily attributed to enhanced incongruent and
487 preferential release of radiogenic Nd during the glacial periods (Jang et al. 2020; Jang et al., 2021; Jang
488 and Nam, 2023). Our study unambiguously demonstrates that both parameters $\Delta\epsilon_{Nd}^{Riv-SPM}$ and degree of
489 Nd adsorption would modulate the particulate ϵ_{Nd} and therefore $\Delta\epsilon_{Nd}^{Leach-Res}$ of marine sediments. Elevated
490 values of $\Delta\epsilon_{Nd}^{Riv-SPM}$ are expected during glacial periods and during the active phase of tectonism when
491 exposure of fresh rocks is more significant, thus favouring incongruent release of Nd isotopes. Thus, the
492 collective impact of high values of $\Delta\epsilon_{Nd}^{Riv-SPM}$ and higher degree Nd adsorption due to lower river water
493 discharge (slowdown of the hydrological cycle) would result in higher particulate ϵ_{Nd} values during the
494 glacial periods. Furthermore, the particle-seawater interaction would result in the release of Nd from the
495 river-borne SPM (Pearce et al., 2013; Jeandel and Oelkers, 2015) having a higher ϵ_{Nd} during the glacial
496 periods and thereby would elevate the seawater ϵ_{Nd} . Therefore, the combined effect of adsorption of
497 dissolved Nd in rivers, increased $\Delta\epsilon_{Nd}^{Riv-SPM}$ and the release of radiogenic Nd from the particulate matter
498 in the oceans would amplify the $\Delta\epsilon_{Nd}^{Leach-Res}$ values of marine sediments during glacial intervals. Thus, the

499 results of our study support the application of $\Delta\epsilon_{\text{Nd}}^{\text{Leach-Res}}$ of marine sediments as a robust tracer to study
500 the weathering records of glacial-interglacial periods.

501 **5. Conclusions**

502 Our investigation of carefully selected two basaltic weathering profiles and re-evaluation of particulate
503 ϵ_{Nd} data of global rivers provide the following important results.

- 504 • Incongruent behaviour of Nd isotopes is unequivocal as evident from differential release of
505 radiogenic Nd to the fluid phase during chemical weathering of basalts. This behaviour is attributed
506 to preferential weathering of minerals having high Sm/Nd ratios and ϵ_{Nd} than the parent basalts.
- 507 • The ϵ_{Nd} values of Nd released to the weathering solutions are reliably captured by the oxyhydroxide
508 phases of weathering profiles via adsorption of Nd from the fluid phases.
- 509 • These two observations and reports of pervasive adsorption of dissolved Nd in rivers led us to
510 hypothesize that particulate ϵ_{Nd} would be sensitive to the degree of Nd adsorption in rivers which in
511 turn be influenced by the discharge-regulated duration of particle-water interaction.
- 512 • Re-evaluation of discharge and particulate ϵ_{Nd} data of the time-series and discrete seasonal data of
513 fourteen rivers of the world from different geographical and climate regimes demonstrate the
514 discharge-dependent ϵ_{Nd} variation, thus supporting the above hypothesis.
- 515 • Evaluation of ϵ_{Nd} differences between high and low discharge periods as a function of seasonal
516 discharge contrast and river lengths indisputably demonstrate that modulation of riverine particulate
517 ϵ_{Nd} is dominantly influenced by the length and duration of adsorption of dissolved Nd.
- 518 • Combined effects of incongruent release of radiogenic Nd, adsorption of dissolved Nd in rivers and
519 riverine SPM-seawater interaction would cause higher ϵ_{Nd} difference between the leachates and

520 residual detrital phases of marine sediments during the glacial periods. Therefore, our investigation
521 advocates the utilization of $\Delta\epsilon_{Nd}^{Leach-Res}$ of marine sediments as a robust tracer of studying glacial-
522 interglacial weathering records.

523

524 **CRedit authorship contribution statement**

525 **Anup Kumar Sharma:** Conceptualization, Investigation, Writing - Original Draft, Project
526 administration, Methodology, Validation, Formal analysis. **Tarun Kumar Dalai:** Conceptualization,
527 Investigation, Writing - Original Draft, Writing - Review & Editing, Resources, Supervision, Project
528 administration, Funding acquisition, Methodology, Validation, Formal analysis. **Prem Chand Kisku:**
529 Resources, Data Curation, Validation, Formal analysis. **Jitendra Kumar Pattanaik:** Resources, Data
530 Curation, Validation, Formal analysis. **Sambuddha Misra:** Writing - Review & Editing, Resources,
531 Validation, Data Curation. **Shivansh Verma:** Resources, Validation, Data Curation. **Anil Dutt Shukla:**
532 Resources, Validation, Data Curation.

533 **Acknowledgements**

534 AKS thanks the Indian Council of Scientific and Industrial Research (CSIR), New Delhi for providing
535 research fellowship (Award no.: 09/921(0229)2019-EMR-I). TKD acknowledges the financial support
536 through the ARF grant from IISER Kolkata.

537 **References**

- 538 Adebayo, S. B., Cui, M., Hong, T., White, C. D., Martin, E. E., Johannesson, K. H., 2018. Rare earth
539 elements geochemistry and Nd isotopes in the Mississippi River and Gulf of Mexico mixing
540 zone. *Frontiers in Marine Science* 5, 166. <https://doi.org/10.3389/fmars.2018.00166>
- 541 Anderson, S. P., Dietrich, W. E., Torres, R., Montgomery, D. R., Loague, K., 1997. Concentration-
542 discharge relationships in runoff from a steep, unchanneled catchment. *Water Resources*
543 *Research* 33, 211-225. <https://doi.org/10.1029/96WR02715>
- 544 Andersson, P. S., Dahlgvist, R., Ingri, J., Gustafsson, O., 2001. The isotopic composition of Nd in a
545 boreal river: a reflection of selective weathering and colloidal transport. *Geochimica et*
546 *Cosmochimica Acta* 65, 521-527. [https://doi.org/10.1016/S0016-7037\(00\)00535-4](https://doi.org/10.1016/S0016-7037(00)00535-4)
- 547 Ashour, R.M., El-Sayed, R., Abdel-Magied, A.F., Abdel-Khalek, A.A., Ali, M.M., Forsberg, K., Uheida,
548 A., Muhammed, M., Dutta, J., 2017. Selective separation of rare earth ions from aqueous solution
549 using functionalized magnetite nanoparticles: kinetic and thermodynamic studies. *Chemical*
550 *Engineering Journal* 327, 286-296. <https://doi.org/10.1016/j.cej.2017.06.101>
- 551 Aubert, D., Stille, P., Probst, A., 2001. REE fractionation during granite weathering and removal by
552 waters and suspended loads: Sr and Nd isotopic evidence. *Geochimica et Cosmochimica Acta* 65,
553 387-406. [https://doi.org/10.1016/S0016-7037\(00\)00546-9](https://doi.org/10.1016/S0016-7037(00)00546-9)
- 554 Aucour, A. M., Tao, F. X., Moreira-Turcq, P., Seyler, P., Sheppard, S., Benedetti, M. F., 2003. The
555 Amazon River: behaviour of metals (Fe, Al, Mn) and dissolved organic matter in the initial mixing
556 at the Rio Negro/Solimões confluence. *Chemical geology* 197, 271-285.
557 [http://dx.doi.org/10.1016/S0009-2541\(02\)00398-4](http://dx.doi.org/10.1016/S0009-2541(02)00398-4)
- 558 Babechuk, M. G., Widdowson, M., Kamber, B. S., 2014. Quantifying chemical weathering intensity and
559 trace element release from two contrasting basalt profiles, Deccan Traps, India. *Chemical*
560 *Geology* 363, 56-75. <http://dx.doi.org/10.1016/j.chemgeo.2013.10.027>
- 561 Babechuk, M. G., Widdowson, M., Murphy, M., Kamber, B. S., 2015. A combined Y/Ho, high field
562 strength element (HFSE) and Nd isotope perspective on basalt weathering, Deccan Traps, India.
563 *Chemical Geology* 396, 25-41. <https://doi.org/10.1016/j.chemgeo.2014.12.017>
- 564 Bai, Jianghao, Kai Luo, Chao Wu, Zhibing Wang, Le Zhang, Shuang Yan, Songxiong Zhong, Jinlong
565 Ma, Gangjian Wei., 2023. Stable neodymium isotopic fractionation during chemical
566 weathering. *Earth and Planetary Science Letters* 617, 118260.
567 <https://doi.org/10.1016/j.epsl.2023.118260>
- 568 Banerjee, A., Chakrabarti, R., Mandal, S., 2016. Geochemical anatomy of a spheroidally weathered
569 diabase. *Chemical Geology* 440, 124-138. <https://doi.org/10.1016/j.chemgeo.2016.07.008>
- 570 Baksi, A. K., 2022. Geochemistry and geochronology of the Rajmahal Flood Basalt Province,
571 northeastern India: Genetic links to Kerguelen hotspot activity. *Journal of Earth System Science*
572 131, 157. <https://doi.org/10.1007/s12040-022-01855-8>

- 573 Bayon, G., Douglas, G. B., Denton, G. J., Monin, L., De Deckker, P., 2020a. Preferential riverine export
574 of fine volcanogenic particles to the southeast Australian margin. *Frontiers in Marine Science* 7, 89.
575 <https://doi.org/10.3389/fmars.2020.00089>
- 576 Bayon, G., Lambert, T., Vigier, N., De Deckker, P., Freslon, N., Jang, K., Larkin, C. S., Piotrowski, A.
577 M., Tachikawa, K., Thollon, M., Tipper, E. T., 2020b. Rare earth element and neodymium isotope
578 tracing of sedimentary rock weathering. *Chemical Geology* 553, 119794.
579 <https://doi.org/10.1016/j.chemgeo.2020.119794>
- 580 Bayon, G., Toucanne, S., Skonieczny, C., André, L., Bermell, S., Cheron, S., Dennielou, B., Etoubleau,
581 J., Freslon, N., Gauchery, T., Germain, Y., Jorry, S. J., Menot, G., Monin, L., Ponzevera, E., Rouget,
582 M. L., Tachikawa, K., Barrat, J. A., 2015. Rare earth elements and neodymium isotopes in world
583 river sediments revisited. *Geochimica et Cosmochimica Acta* 170, 17-38.
584 <https://doi.org/10.1016/j.gca.2015.08.001>
- 585 Bouchez, J., Gaillardet, J., France-Lanord, C., Maurice, L., Dutra-Maia, P., 2011. Grain size control of
586 river suspended sediment geochemistry: Clues from Amazon River depth profiles. *Geochem.*
587 *Geophys. Geosys.* 12. <http://dx.doi.org/10.1029/2010GC003380>
- 588 Briao, G. D. V., da Silva, M. G. C., Vieira, M. G. A., 2021. Efficient and selective adsorption of
589 neodymium on expanded vermiculite. *Industrial & Engineering Chemistry Research* 60, 4962-4974.
590 <https://doi.org/10.1021/acs.iecr.0c05979>
- 591 Chatterjee, J., Singh S. K., 2014. Dissolved Nd in the Ganga River system and its flux to the Bay of
592 Bengal, Goldschmidt abstracts. <https://goldschmidtabstracts.info/2014/387.pdf>
- 593 Chen, T. Y., Frank, M., Haley, B. A., Gutjahr, M., Spielhagen, R. F., 2012. Variations of North Atlantic
594 inflow to the central Arctic Ocean over the last 14 million years inferred from hafnium and
595 neodymium isotopes. *Earth and Planetary Science Letters* 353, 82-92.
596 <https://doi.org/10.1016/j.epsl.2012.08.012>
- 597 Ciffroy, P., Reyss, J. L., Siclet, F., 2003. Determination of the residence time of suspended particles in
598 the turbidity maximum of the Loire estuary by ⁷Be analysis. *Estuarine, Coastal and Shelf*
599 *Science* 57, 553-568. [https://doi.org/10.1016/S0272-7714\(02\)00339-6](https://doi.org/10.1016/S0272-7714(02)00339-6)
- 600 Clow, D. W., Mast, M. A., 2010. Mechanisms for chemostatic behavior in catchments: Implications for
601 CO₂ consumption by mineral weathering. *Chemical Geology* 269, 40-51.
602 <http://dx.doi.org/10.1016/j.chemgeo.2009.09.014>
- 603 Dai, A., Trenberth, K. E., 2002. Estimates of freshwater discharge from continents: Latitudinal and
604 seasonal variations. *Journal of hydrometeorology* 3, 660-687. [https://doi.org/10.1175/1525-7541\(2002\)003%3C0660:EOFDFC%3E2.0.CO;2](https://doi.org/10.1175/1525-7541(2002)003%3C0660:EOFDFC%3E2.0.CO;2)
- 606 Dang, D. H., Ha, Q. K., Némery, J., Strady, E., 2023. The seasonal variations in the interactions between
607 rare earth elements and organic matter in tropical rivers. *Chemical Geology* 638, 121711.
608 <https://doi.org/10.1016/j.chemgeo.2023.121711>

- 609 Dausmann, V., Gutjahr, M., Frank, M., Kouzmanov, K., Schaltegger, U., 2019. Experimental evidence
610 for mineral-controlled release of radiogenic Nd, Hf and Pb isotopes from granitic rocks during
611 progressive chemical weathering. *Chemical Geology* 507, 64-84.
612 <https://doi.org/10.1016/j.chemgeo.2018.12.024>
- 613 Davranche, M., Pourret, O., Gruau, G., Dia, A., Le Coz-Bouhnik, M., 2005. Adsorption of REE (III)-
614 humate complexes onto MnO₂: Experimental evidence for cerium anomaly and lanthanide tetrad
615 effect suppression. *Geochimica et Cosmochimica Acta* 69, 4825-4835.
616 <https://doi.org/10.1016/j.gca.2005.06.005>
- 617 Do, A. T., Sottolichio, A., Huybrechts, N., Gardel, A., 2020. Circulation patterns and implication for fine
618 sediment transport in a preserved tropical estuary: The case of the Maroni (French
619 Guiana). *Regional studies in marine science* 40, 101493.
620 <https://doi.org/10.1016/j.rsma.2020.101493>
- 621 Elderfield, H., Greaves, M. J., 1982. The rare earth elements in seawater. *Nature* 296, 214-219.
622 <https://doi.org/10.1038/296214a0>
- 623 Elderfield, H., Upstill-Goddard, R., Sholkovitz, E. R., 1990. The rare earth elements in rivers, estuaries,
624 and coastal seas and their significance to the composition of ocean waters. *Geochimica et*
625 *Cosmochimica Acta* 54, 971-991. [https://doi.org/10.1016/0016-7037\(90\)90432-K](https://doi.org/10.1016/0016-7037(90)90432-K)
- 626 Fee, J. A., Gaudette, H. E., Lyons, W. B., Long, D. T., 1992. Rare-earth element distribution in Lake
627 Tyrrell groundwaters, Victoria, Australia. *Chemical geology* 96, 67-93.
628 [https://doi.org/10.1016/0009-2541\(92\)90122-L](https://doi.org/10.1016/0009-2541(92)90122-L)
- 629 Garcon, M., Chauvel, C., 2014. Where is basalt in river sediments, and why does it matter? *Earth and*
630 *Planetary Science Letters* 407, 61-69. <https://doi.org/10.1016/j.epsl.2014.09.033>
- 631 Garcon, M., Chauvel, C., France-Lanord, C., Limonta, M., Garzanti, E., 2014. Which minerals control
632 the Nd–Hf–Sr–Pb isotopic compositions of river sediments? *Chemical Geology* 364, 42-55.
633 <https://doi.org/10.1016/j.chemgeo.2013.11.018>
- 634 Garzanti, E., Ando, S., France-Lanord, C., Censi, P., Vignola, P., Galy, V., Lupker, M., 2011.
635 Mineralogical and chemical variability of fluvial sediments 2. Suspended-load silt (Ganga–
636 Brahmaputra, Bangladesh). *Earth and Planetary Science Letters* 302, 107-120.
637 <https://doi.org/10.1016/j.epsl.2010.11.043>
- 638 Goldstein, S. J., Jacobsen, S. B., 1987. The Nd and Sr isotopic systematics of river-water dissolved
639 material: Implications for the sources of Nd and Sr in seawater. *Chemical Geology: Isotope*
640 *Geoscience section* 66, 245-272. [https://doi.org/10.1016/0168-9622\(87\)90045-5](https://doi.org/10.1016/0168-9622(87)90045-5)
- 641 Goldstein, S. J., Jacobsen, S. B., 1988. Nd and Sr isotopic systematics of river water suspended material:
642 implications for crustal evolution. *Earth and Planetary Science Letters* 87, 249-265.
643 [https://doi.org/10.1016/0012-821X\(88\)90013-1](https://doi.org/10.1016/0012-821X(88)90013-1)

- 644 Goldstein, S. L., O’Nions, R. K., Hamilton, P. J., 1984. A Sm-Nd isotopic study of atmospheric dusts
645 and particulates from major river systems. *Earth and planetary Science letters* 70, 221-236.
646 [https://doi.org/10.1016/0012-821X\(84\)90007-4](https://doi.org/10.1016/0012-821X(84)90007-4)
- 647 Gupta S. K., Chen K. Y., 1975. Partitioning of trace metals in selective chemical fractions of near shore
648 sediments. *Environmental Letters* 10, 129. <https://doi.org/10.1080/00139307509435816>
- 649 Harvey, J. W., Wagner, B. J., Bencala, K. E., 1996. Evaluating the reliability of the stream tracer
650 approach to characterize stream-subsurface water exchange. *Water resources research* 32, 2441-
651 2451. <http://dx.doi.org/10.1029/96WR01268>
- 652 Henry, F., Probst, J. L., Thouron, D., Depetris, P., Garçon, V., 1996. Nd-Sr isotopic compositions of
653 dissolved and particulate material transported by the Parana and Uruguay rivers during high
654 (December 1993) and low (September 1994) water periods. *Geological Sciences, Bulletins and
655 Memoirs* 49, 89-100.
- 656 Hindshaw, R. S., Aciego, S. M., Piotrowski, A. M., Tipper, E. T., 2018. Decoupling of dissolved and
657 bedrock neodymium isotopes during sedimentary cycling. *Geochemical Perspectives Letters* 8, 43-
658 46. <https://doi.org/10.7185/geochemlet.1828>
- 659 Hindshaw, R. S., Teisserenc, R., Le Dantec, T., Tananaev, N., 2019. Seasonal change of geochemical
660 sources and processes in the Yenisei River: A Sr, Mg and Li isotope study. *Geochimica et
661 Cosmochimica Acta* 255, 222-236. <https://doi.org/10.1016/j.gca.2019.04.015>
- 662 Horbe, A. M. C., Albuquerque, M. F. D. S., Dantas, E. L., 2022. Nd and Sr Isotopes and REE
663 Investigation in Tropical Weathering Profiles of Amazon Region. *Frontiers in Earth Science* 10,
664 845224. <https://doi.org/10.3389/feart.2022.845224>
- 665 Ibarra, D. E., Caves, J. K., Moon, S., Thomas, D. L., Hartmann, J., Chamberlain, C. P., Maher, K., 2016.
666 Differential weathering of basaltic and granitic catchments from concentration–discharge
667 relationships. *Geochimica et Cosmochimica Acta* 190, 265-293.
668 <https://doi.org/10.1016/j.gca.2016.07.006>
- 669 Ingri, J., Widerlund, A., 1994. Uptake of alkali and alkaline-earth elements on suspended iron and
670 manganese in the Kalix River, northern Sweden. *Geochimica et Cosmochimica Acta* 58, 5433-5442.
671 [https://doi.org/10.1016/0016-7037\(94\)90240-2](https://doi.org/10.1016/0016-7037(94)90240-2)
- 672 Ingri, J., Widerlund, A., Land, M., Gustafsson, Ö., Andersson, P., Ohlander, B. (2000) Temporal
673 variations in the fractionation of the rare earth elements in a boreal river; the role of colloidal
674 particles. *Chemical Geology* 166, 23-45. [https://doi.org/10.1016/S0009-2541\(99\)00178-3](https://doi.org/10.1016/S0009-2541(99)00178-3)
- 675 Jang, K., Ahn, Y., Joe, Y.J., Braun, C.A., Joo, Y.J., Kim, J.H., Bayon, G., Forwick, M., Vogt, C., Nam,
676 S.I., 2021. Glacial and environmental changes in northern Svalbard over the last 16.3 ka inferred
677 from neodymium isotopes. *Global and Planetary Change* 201, 103483.
678 <https://doi.org/10.1016/j.gloplacha.2021.103483>
- 679 Jang, K., Bayon, G., Han, Y., Joo, Y. J., Kim, J. H., Ryu, J. S., Woo, J., Forwick, M., Szczuciński, W.,
680 Kim, J. H., Nam, S. I., 2020. Neodymium isotope constraints on chemical weathering and past

- 681 glacial activity in Svalbard. *Earth and Planetary Science Letters* 542, 116319.
682 <https://doi.org/10.1016/j.epsl.2020.116319>
- 683 Jang, K., Bayon, G., Han, Y., Joo, Y. J., Kim, J. H., Ryu, J. S., Woo, J., Forwick, M., Szczuciński, W.,
684 Kim, J. H., Nam, S. I., 2020b. Neodymium isotope constraints on chemical weathering and past
685 glacial activity in Svalbard. *Earth and Planetary Science Letters* 542, 116319.
686 <https://doi.org/10.1016/j.epsl.2020.116319>
- 687 Jang, K., Nam, S. I., 2023 Application of Sedimentary Neodymium Isotopes to the Reconstruction of the
688 Arctic Paleoceanography. *Ocean and Polar Research* 45, 89-102.
689 <https://doi.org/10.4217/OPR.2023005>
- 690 Jeandel, C., Oelkers, E. H., 2015. The influence of terrigenous particulate material dissolution on ocean
691 chemistry and global element cycles. *Chemical Geology* 395, 50-66.
692 <https://doi.org/10.1016/j.chemgeo.2014.12.001>
- 693 Jian, X., Yang, S., Hong, D., Liang, H., Zhang, S., Fu, H., Zhang, W., 2020a. Seasonal geochemical
694 heterogeneity of sediments from a subtropical mountainous river in SE China. *Marine Geology* 422,
695 106120. <https://doi.org/10.1016/j.margeo.2020.106120>
- 696 Jian, X., Zhang, W., Yang, S., Kao, S. J., 2020b. Climate-dependent sediment composition and transport
697 of mountainous rivers in tectonically stable, subtropical East Asia. *Geophysical Research*
698 *Letters* 47, e2019GL086150. <https://doi.org/10.1029/2019GL086150>
- 699 Johansson, H., Jonsson, K., Forsman, K. J., Worman, A., 2001. Retention of conservative and sorptive
700 solutes in streams—simultaneous tracer experiments. *Science of the total environment* 266, 229-
701 238. [https://doi.org/10.1016/S0048-9697\(00\)00758-0](https://doi.org/10.1016/S0048-9697(00)00758-0)
- 702 Kisku, P. C., Kumar, H., Pattanaik, J. K., 2020. Hydrogeochemical Study of Morang River Draining
703 Rajmahal Basalt: Implication to Mineral Equilibria and Chemical Weathering. *Proceedings of the*
704 *Indian National Science Academy* 86, 1239-1257. <http://dx.doi.org/10.16943/ptinsa/2020/155493>
- 705 Land, M., Ohlander, B., Ingri, J., Thunberg, J., 1999. Solid speciation and fractionation of rare earth
706 elements in a spodosol profile from northern Sweden as revealed by sequential extraction. *Chemical*
707 *Geology* 160, 121-138. [https://doi.org/10.1016/S0009-2541\(99\)00064-9](https://doi.org/10.1016/S0009-2541(99)00064-9)
- 708 Larkin, C.S., Piotrowski, A.M., Hindshaw, R.S., Bayon, G., Hilton, R.G., Baronas, J.J., Dellinger, M.,
709 Wang, R., Tipper, E.T., 2021. Constraints on the source of reactive phases in sediment from a major
710 Arctic River using neodymium isotopes. *Earth and Planetary Science Letters* 565,
711 p.116933. <https://doi.org/10.1016/j.epsl.2021.116933>
- 712 Lei, H. L., Yang, T., Jiang, S. Y., Pu, W., 2019. A simple two-stage column chromatographic separation
713 scheme for strontium, lead, neodymium and hafnium isotope analyses in geological samples by
714 thermal ionization mass spectrometry or multi-collector inductively coupled plasma mass
715 spectrometry. *Journal of Separation Science* 42, 3261-3275. <https://doi.org/10.1002/jssc.201900579>
- 716 Leybourne, M. I., Cousens, B. L., 2005. Rare earth elements (REE) and Nd and Sr isotopes in
717 groundwater and suspended sediments from the Bathurst Mining Camp, New Brunswick: water-

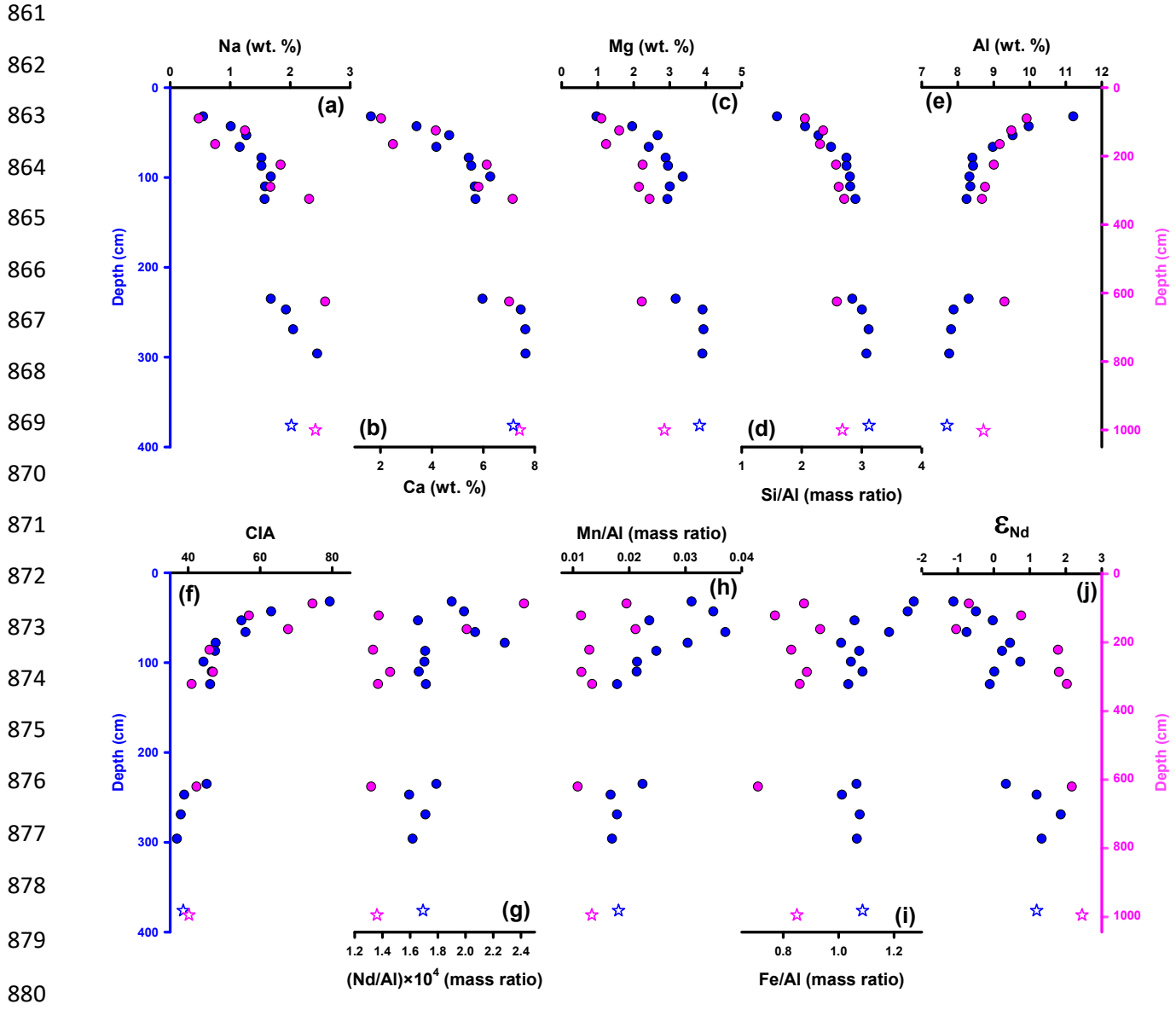
- 718 rock reactions and elemental fractionation. *Rare Earth Elements in Groundwater Flow Systems*,
719 253-293. https://doi.org/10.1007/1-4020-3234-X_10
- 720 Liu, H., Guo, H., Pourret, O., Chen, Y., Yuan, R., 2019. Role of manganese oxyhydroxides in the
721 transport of rare earth elements along a groundwater flow path. *International journal of*
722 *environmental research and public health* 16, 2263. <https://doi.org/10.3390/ijerph16132263>
- 723 Liu, X. M., Rudnick, R. L., McDonough, W. F., Cummings, M. L., 2013. Influence of chemical
724 weathering on the composition of the continental crust: Insights from Li and Nd isotopes in bauxite
725 profiles developed on Columbia River Basalts. *Geochimica et Cosmochimica Acta* 115, 73-91.
726 <http://dx.doi.org/10.1016/j.gca.2013.03.043>
- 727 Liu-Lu, B., Jin, Z., Gou, L. F., Zhang, F., He, M. Y., Xu, Y., 2022. Seasonal River chemistry and lithium
728 isotopes in the Min Jiang at eastern Tibetan Plateau: roles of silicate weathering and hydrology.
729 *Frontiers in Earth Science* 10, 838867. <https://doi.org/10.3389/feart.2022.838867>
- 730 Ma, J. L., Wei, G. J., Xu, Y. G., Long, W. G., Sun, W. D., 2007. Mobilization and re-distribution of major
731 and trace elements during extreme weathering of basalt in Hainan Island, South China. *Geochimica*
732 *et Cosmochimica Acta* 71, 3223-3237. <https://doi.org/10.1016/j.gca.2007.03.035>
- 733 Ma, J., Wei, G., Xu, Y., Long, W., 2010. Variations of Sr–Nd–Hf isotopic systematics in basalt during
734 intensive weathering. *Chemical Geology* 269, 376-385.
735 <https://doi.org/10.1016/j.chemgeo.2009.10.012>
- 736 Manaka, T., Araoka, D., Yoshimura, T., Hossain, H. Z., Nishio, Y., Suzuki, A., Kawahata, H., 2017.
737 Downstream and seasonal changes of lithium isotope ratios in the Ganges-Brahmaputra River
738 system. *Geochemistry, Geophysics, Geosystems* 18, 3003-3015.
739 https://ui.adsabs.harvard.edu/link_gateway/2017GGG....18.3003M/doi:10.1002/2016GC006738
- 740 Martin, C. E., McCulloch, M. T., 1999. Nd-Sr isotopic and trace element geochemistry of river
741 sediments and soils in a fertilized catchment, New South Wales, Australia. *Geochimica et*
742 *Cosmochimica Acta* 63, 287-305. [https://doi.org/10.1016/S0016-7037\(98\)00308-1](https://doi.org/10.1016/S0016-7037(98)00308-1)
- 743 McGuire, K. J., McDonnell, J. J., 2006. A review and evaluation of catchment transit time
744 modeling. *Journal of Hydrology* 330, 543-563. <https://doi.org/10.1016/j.jhydrol.2006.04.020>
- 745 Merschel, G., Bau, M., Schmidt, K., Münker, C., Dantas, E. L., 2017. Hafnium and neodymium isotopes
746 and REY distribution in the truly dissolved, nanoparticulate/colloidal and suspended loads of rivers
747 in the Amazon Basin, Brazil. *Geochimica et Cosmochimica Acta* 213, 383-399.
748 <https://doi.org/10.1016/j.gca.2017.07.006>
- 749 Moquet, J.S., Morera, S., Turcq, B., Poitrasson, F., Roddaz, M., Moreira-Turcq, P., Espinoza, J.C.,
750 Guyot, J.L., Takahashi, K., Orrillo-Vigo, J., Petrick, S., Mounic, S., Sondag, F., 2020. Control of
751 seasonal and inter-annual rainfall distribution on the Strontium-Neodymium isotopic compositions
752 of suspended particulate matter and implications for tracing ENSO events in the Pacific coast
753 (Tumbes basin, Peru). *Global and Planetary Change* 185, 103080.
754 <https://doi.org/10.1016/j.gloplacha.2019.103080>

- 755 Mosai, A. K., Chimuka, L., Cukrowska, E. M., Kotzé, I. A., Tutu, H., 2019. The recovery of rare earth
756 elements (REEs) from aqueous solutions using natural zeolite and bentonite. *Water, Air, & Soil*
757 *Pollution* 230, 1-17. <https://doi.org/10.1007/s11270-019-4236-4>
- 758 Negrel, P., 2006. Water–granite interaction: clues from strontium, neodymium and rare earth elements in
759 soil and waters. *Applied Geochemistry* 21, 1432-1454.
760 <https://doi.org/10.1016/j.apgeochem.2006.04.007>
- 761 Negrel, P., Casanova, J., Blomqvist, R., 2001. Nd isotopes and water mixing phenomena in
762 groundwaters from Palmottu (Finland). *Water research*, 35, 1617-1623.
763 [https://doi.org/10.1016/S0043-1354\(00\)00569-8](https://doi.org/10.1016/S0043-1354(00)00569-8)
- 764 Neidhardt, H., Berner, Z.A., Freikowski, D., Biswas, A., Majumder, S., Winter, J., Gallert, C.,
765 Chatterjee, D., Norra, S., 2014. Organic carbon induced mobilization of iron and manganese in a
766 West Bengal aquifer and the muted response of groundwater arsenic concentrations. *Chemical*
767 *Geology* 367, 51-62. <https://doi.org/10.1016/j.chemgeo.2013.12.021>
- 768 Nobre Silva, I. G., Weis, D., Scoates, J. S., 2010. Effects of acid leaching on the Sr-Nd-Hf isotopic
769 compositions of ocean island basalts. *Geochem. Geophys. Geosys.* 11,
770 <https://doi.org/10.1029/2010GC003176>
- 771 Ohlander, B., Ingri, J., Land, M., Schöberg, H., 2000. Change of Sm-Nd isotope composition during
772 weathering of till. *Geochimica et Cosmochimica Acta* 64, 813-820. [https://doi.org/10.1016/S0016-7037\(99\)00365-8](https://doi.org/10.1016/S0016-7037(99)00365-8)
773
- 774 Palmer, M. R., Edmond, J. M., 1993. Uranium in river water. *Geochimica et Cosmochimica Acta* 57,
775 4947-4955. [https://doi.org/10.1016/0016-7037\(93\)90131-F](https://doi.org/10.1016/0016-7037(93)90131-F)
- 776 Pearce, C. R., Jones, M. T., Oelkers, E. H., Pradoux, C., Jeandel, C., 2013. The effect of particulate
777 dissolution on the neodymium (Nd) isotope and Rare Earth Element (REE) composition of
778 seawater. *Earth and Planetary Science Letters* 369, 138-147.
779 <https://doi.org/10.1016/j.epsl.2013.03.023>
- 780 Peucker-Ehrenbrink, B., Miller, M. W., Arsouze, T., Jeandel, C., 2010 Continental bedrock and riverine
781 fluxes of strontium and neodymium isotopes to the oceans. *Geochem. Geophys. Geosys.* 11.
782 <https://doi.org/10.1029/2009GC002869>
- 783 Piegras, D. J., Wasserburg, G. J., Dasch, E. J., 1979. The isotopic composition of Nd in different ocean
784 masses. *Earth and Planetary Science Letters* 45, 223-236. [https://doi.org/10.1016/0012-821X\(79\)90125-0](https://doi.org/10.1016/0012-821X(79)90125-0)
785
- 786 Rickli, J., Frank, M., Stichel, T., Georg, R. B., Vance, D., Halliday, A. N., 2013. Controls on the
787 incongruent release of hafnium during weathering of metamorphic and sedimentary
788 catchments. *Geochimica et Cosmochimica Acta* 101, 263-284.
789 <http://dx.doi.org/10.1016/j.gca.2012.10.019>
- 790 Rousseau, T. C., Roddaz, M., Moquet, J. S., Delgado, H. H., Calves, G., Bayon, G., 2019. Controls on
791 the geochemistry of suspended sediments from large tropical South American rivers (Amazon,

- 792 Orinoco and Maroni). *Chemical Geology* 522, 38-54.
793 <https://doi.org/10.1016/j.chemgeo.2019.05.027>
- 794 Shiller, A. M., 2002. Seasonality of dissolved rare earth elements in the lower Mississippi
795 River. *Geochemistry, Geophysics, Geosystems* 3, 1-14. <https://doi.org/10.1029/2002GC000372>
- 796 Sholkovitz, E. R., 1995. The aquatic chemistry of rare earth elements in rivers and estuaries. *Aquatic*
797 *geochemistry* 1, 1-34. <https://doi.org/10.1007/BF01025229>
- 798 Smith, C., Liu, X. M., 2018. Spatial and temporal distribution of rare earth elements in the Neuse River,
799 North Carolina. *Chemical Geology* 488, 34-43. <https://doi.org/10.1016/j.chemgeo.2018.04.003>
- 800 Spencer, K. J., De Carlo, E. H., McMurtry, G. M., 1996. Isotopic clues to sources of natural and
801 anthropogenic lead in sediments and soils from O'ahu, Hawai'i. *Pacific Sci.* 49, 492-510.
802 <http://hdl.handle.net/10125/2336>
- 803 Sprenger, M., Stumpp, C., Weiler, M., Aeschbach, W., Allen, S.T., Benettin, P., Dubbert, M., Hartmann,
804 A., Hrachowitz, M., Kirchner, J.W., McDonnell, J.J., 2019. The demographics of water: A review of
805 water ages in the critical zone. *Reviews of Geophysics* 57, 800-834.
806 <https://doi.org/10.1029/2018RG000633>
- 807 Steinmann, M., Stille, P., 2008. Controls on transport and fractionation of the rare earth elements in
808 stream water of a mixed basaltic-granitic catchment basin (Massif Central, France). *Chemical*
809 *Geology* 254, 1-18. <https://doi.org/10.1016/j.chemgeo.2008.04.004>
- 810 Sufke, F., Gutjahr, M., Gilli, A., Anselmetti, F. S., Glur, L., Eisenhauer, A., 2019. Early-stage weathering
811 systematics of Pb and Nd isotopes derived from a high-Alpine Holocene Lake sediment
812 record. *Chemical geology* 507, 42-53. <https://doi.org/10.1016/j.chemgeo.2018.12.026>
- 813 Tachikawa, K., Roy-Barman, M., Michard, A., Thouron, D., Yeghicheyan, D., Jeandel, C., 2004.
814 Neodymium isotopes in the Mediterranean Sea: Comparison between seawater and sediment
815 signals. *Geochimica et Cosmochimica Acta* 68, 3095-3106.
816 <https://doi.org/10.1016/j.gca.2004.01.024>
- 817 Tanaka, T., Togashi, S., Kamioka, H., Amakawa, H., Kagami, H., Hamamoto, T., Yuhara, M., Orihashi,
818 Y., Yoneda, S., Shimizu, H., Kunimaru, T., 2000. JNdi-1: a neodymium isotopic reference in
819 consistency with LaJolla neodymium. *Chemical Geology* 168, 279-281.
820 [https://doi.org/10.1016/S0009-2541\(00\)00198-4](https://doi.org/10.1016/S0009-2541(00)00198-4)
- 821 Tipper, E.T., Stevenson, E.I., Alcock, V., Knight, A.C., Baronas, J.J., Hilton, R.G., Bickle, M.J., Larkin,
822 C.S., Feng, L., Relph, K.E., Hughes, G., 2021. Global silicate weathering flux overestimated
823 because of sediment-water cation exchange. *Proceedings of the National Academy of Sciences* 118,
824 e2016430118. <https://doi.org/10.1073/pnas.2016430118>
- 825 Tricca, A., Stille, P., Steinmann, M., Kiefel, B., Samuel, J., Eikenberg, J., 1999. Rare earth elements and
826 Sr and Nd isotopic compositions of dissolved and suspended loads from small river systems in the
827 Vosges mountains (France), the river Rhine and groundwater. *Chemical Geology* 160, 139-158.
828 [https://doi.org/10.1016/S0009-2541\(99\)00065-0](https://doi.org/10.1016/S0009-2541(99)00065-0)

- 829 Viers, J., Roddaz, M., Filizola, N., Guyot, J.L., Sondag, F., Brunet, P., Zouiten, C., Boucayrand, C.,
830 Martin, F., Boaventura, G.R., 2008. Seasonal and provenance controls on Nd–Sr isotopic
831 compositions of Amazon rivers suspended sediments and implications for Nd and Sr fluxes
832 exported to the Atlantic Ocean. *Earth and Planetary Science Letters* 274, 511-523.
833 <https://doi.org/10.1016/j.epsl.2008.08.011>
- 834 Viers, J., Wasserburg, G. J., 2004. Behavior of Sm and Nd in a lateritic soil profile. *Geochimica et*
835 *Cosmochimica Acta* 68, 2043-2054. <https://doi.org/10.1016/j.gca.2003.10.034>
- 836 Wallbrink, P. J., Murray, A. S., Olley, J. M., Olive, L. J., 1998. Determining sources and transit times of
837 suspended sediment in the Murrumbidgee River, New South Wales, Australia, using fallout ^{137}Cs
838 and ^{210}Pb . *Water Resources Research* 34, 879-887. <https://doi.org/10.1029/97WR03471>
- 839 Wallrich, I. L., Stewart, B. W., Capo, R. C., Hedin, B. C., Phan, T. T., 2020. Neodymium isotopes track
840 sources of rare earth elements in acidic mine waters. *Geochimica et Cosmochimica Acta*, 269, 465-
841 483. <https://doi.org/10.1016/j.gca.2019.10.044>
- 842 Weis, D., Kieffer, B., Maerschalk, C., Barling, J., De Jong, J., Williams, G. A., Hanano, D., Pretorius,
843 W., Mattielli, N., Scoates, J. S., Goolaerts, A., 2006. High-precision isotopic characterization of
844 USGS reference materials by TIMS and MC-ICP-MS. *Geochemistry Geophysics Geosystems* 7, 8.
845 <https://doi.org/10.1029/2006GC001283>
- 846 Wilson, D. J., Piotrowski, A. M., Galy, A., Clegg, J. A., 2013. Reactivity of neodymium carriers in deep
847 sea sediments: Implications for boundary exchange and paleoceanography. *Geochimica et*
848 *Cosmochimica Acta* 109, 197-221. <https://doi.org/10.1016/j.gca.2013.01.042>
- 849 Worman, A., 1998. Analytical solution and timescale for transport of reacting solutes in rivers and
850 streams. *Water Resources Research* 34, 2703-2716. <https://doi.org/10.1029/98WR01338>
- 851 Worman, A., Forsman, J., Johansson, H., 1998. Modeling retention of sorbing solutes in streams based
852 on tracer experiment using ^{51}Cr . *Journal of environmental engineering* 124, 122-130.
853 [https://doi.org/10.1061/\(ASCE\)0733-9372\(1998\)124:2\(122\)](https://doi.org/10.1061/(ASCE)0733-9372(1998)124:2(122))
- 854 Zhang, F., Dellinger, M., Hilton, R. G., Yu, J., Allen, M. B., Densmore, A. L., Jin, Z., 2022. Hydrological
855 control of river and seawater lithium isotopes. *Nature Communications* 13, 3359.
856 <https://doi.org/10.1038/s41467-022-31076-y>
- 857 Zhong, J., Li, S. L., Tao, F., Ding, H., Liu, J., 2017. Impacts of hydrologic variations on chemical
858 weathering and solute sources in the Min River basin, Himalayan–Tibetan region. *Environmental*
859 *Science and Pollution Research* 24, 19126-19137. <https://doi.org/10.1007/s11356-017-9584-2>

860 **Figures**



881 **Fig. 1.** Signatures of weathering and post-weathering processes (adsorption) with depth in the
 882 Dalahi (blue) and Pakuria (pink) weathering profiles. **(a-d):** Chemical weathering drives drop in
 883 concentrations of Na, Ca, Mg and Si/Al ratio relative to the parent basalts (stars). **(e):** The
 884 concentrations of the immobile element Al, as expected, show increasing upward trends during
 885 weathering. **(f):** Progressive chemical weathering is evident from upward increasing values of
 886 CIA, consistent with the loss of mobile elements (Na, Ca, Mg and Si). **(g, h, i):** The upward
 887 increasing Nd/Al ratios display a general correspondence with Fe/Al and Mn/Al ratios,
 888 indicating adsorption of Nd from fluid phase onto oxyhydroxide phases. **(j):** The incongruent
 889 behaviour of Nd isotopes during weathering, evident from the upward decreasing trend of ϵ_{Nd} is
 890 most likely driven by differential mineral weathering (see Fig. 2 and text for more details).

891
892
893
894
895
896
897
898
899
900
901
902
903
904
905
906
907
908
909
910
911
912
913
914
915

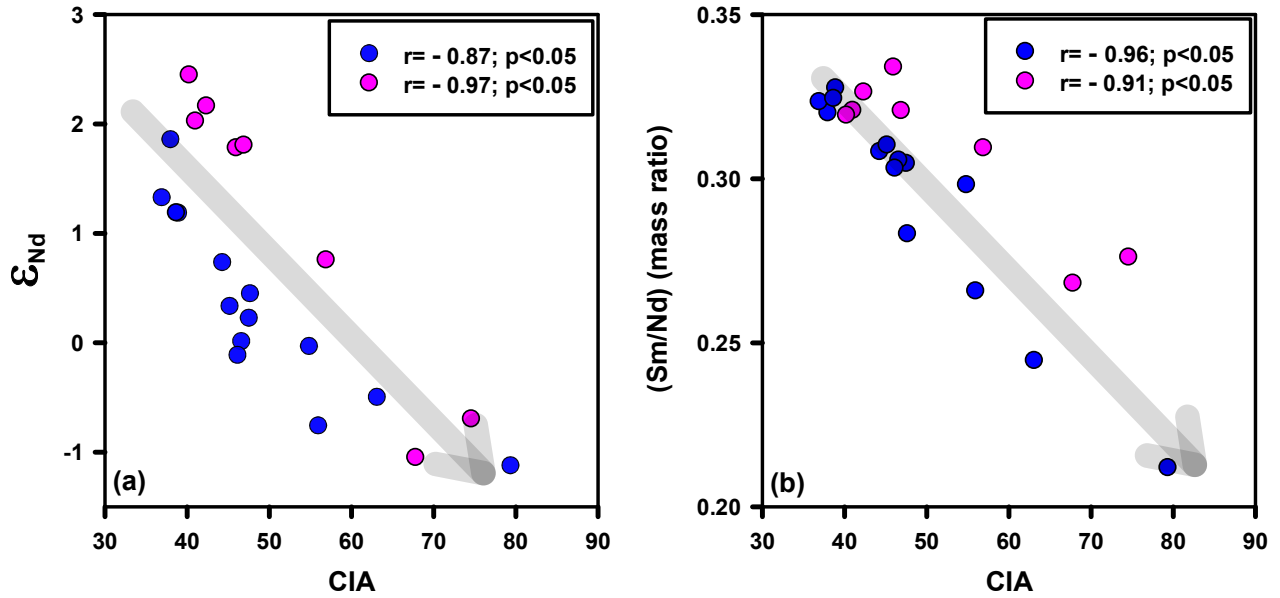


Fig. 2. Incongruent behaviour of Sm, Nd and its isotopes during weathering. The strong inverse correlations of ϵ_{Nd} (a) and Sm/Nd ratio (b) with CIA in the Dalahi (blue) and Pakuria (pink) profiles are suggestive of preferential weathering of minerals having higher Sm/Nd ratio and ϵ_{Nd} compared to the basaltic parent rocks. The directions of increasing degree of chemical weathering are marked with arrows.

916
917
918
919
920
921
922
923
924
925
926
927
928
929
930
931
932
933
934
935
936
937
938
939
940
941
942
943
944

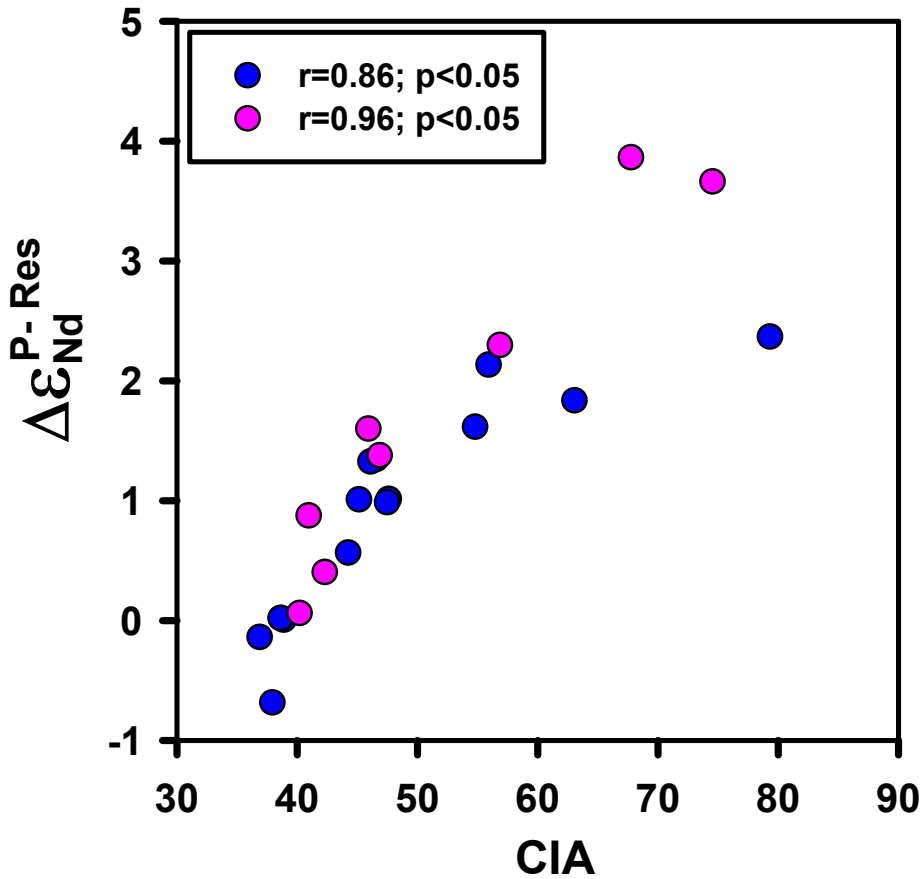


Fig. 3. The incongruent loss of radiogenic Nd to solution during progressive chemical weathering. The ϵ_{Nd} difference between the parent basalts and the residual phases (Supplementary Note SN4) of the profiles ($\Delta\epsilon_{Nd}^{P-Res}$) is a measure of ϵ_{Nd} of the weathering solution. The $\Delta\epsilon_{Nd}^{P-Res}$ scales with the degree of weathering as evident from its positive correlation with CIA.

945
946
947
948
949
950
951
952
953
954
955
956
957
958
959
960
961
962
963
964
965
966
967
968
969
970
971
972
973

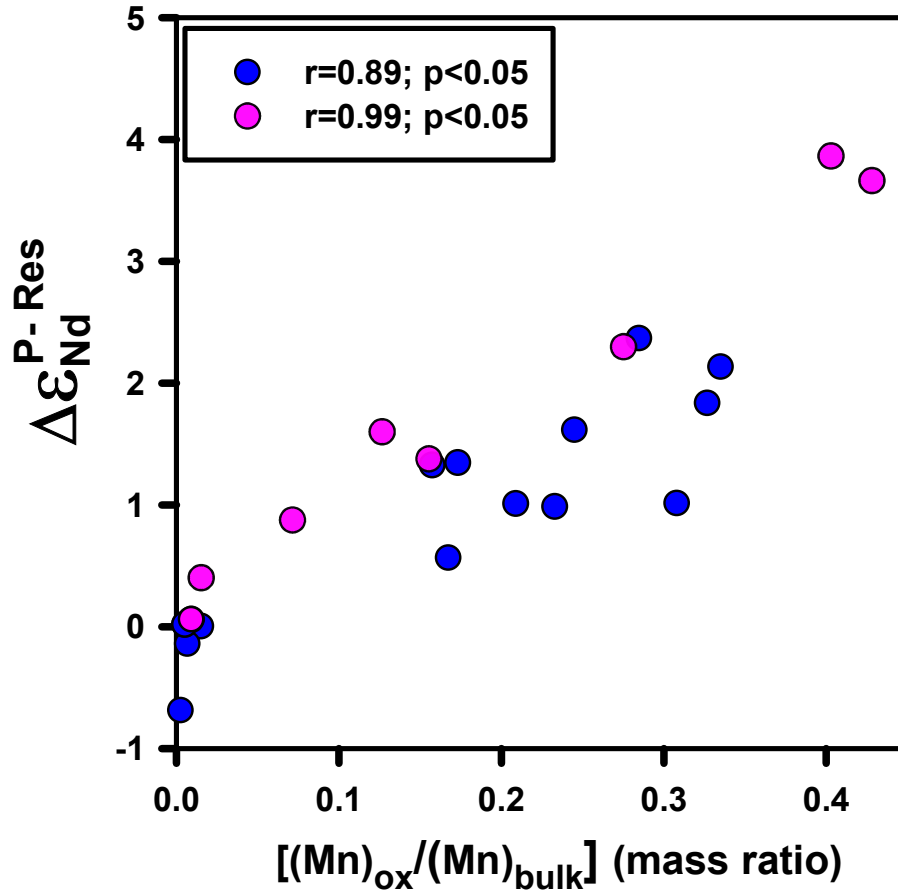


Fig. 4. Oxyhydroxide phases capture ϵ_{Nd} of Nd released to the weathering solution. The ϵ_{Nd} of weathering solutions ($\Delta\epsilon_{\text{Nd}}^{\text{P-Res}}$) is recorded in Mn oxyhydroxide phases as evident from strong positive correlations observed between $\Delta\epsilon_{\text{Nd}}^{\text{P-Res}}$ and ratio of Mn concentrations in the oxyhydroxide to bulk phases ($[\text{Mn}]_{\text{ox}}/[\text{Mn}]_{\text{bulk}}$).

974
 975
 976
 977
 978
 979
 980
 981
 982
 983
 984
 985
 986
 987
 988
 989
 990
 991
 992
 993
 994
 995
 996
 997
 998
 999
 1000
 1001
 1002
 1003

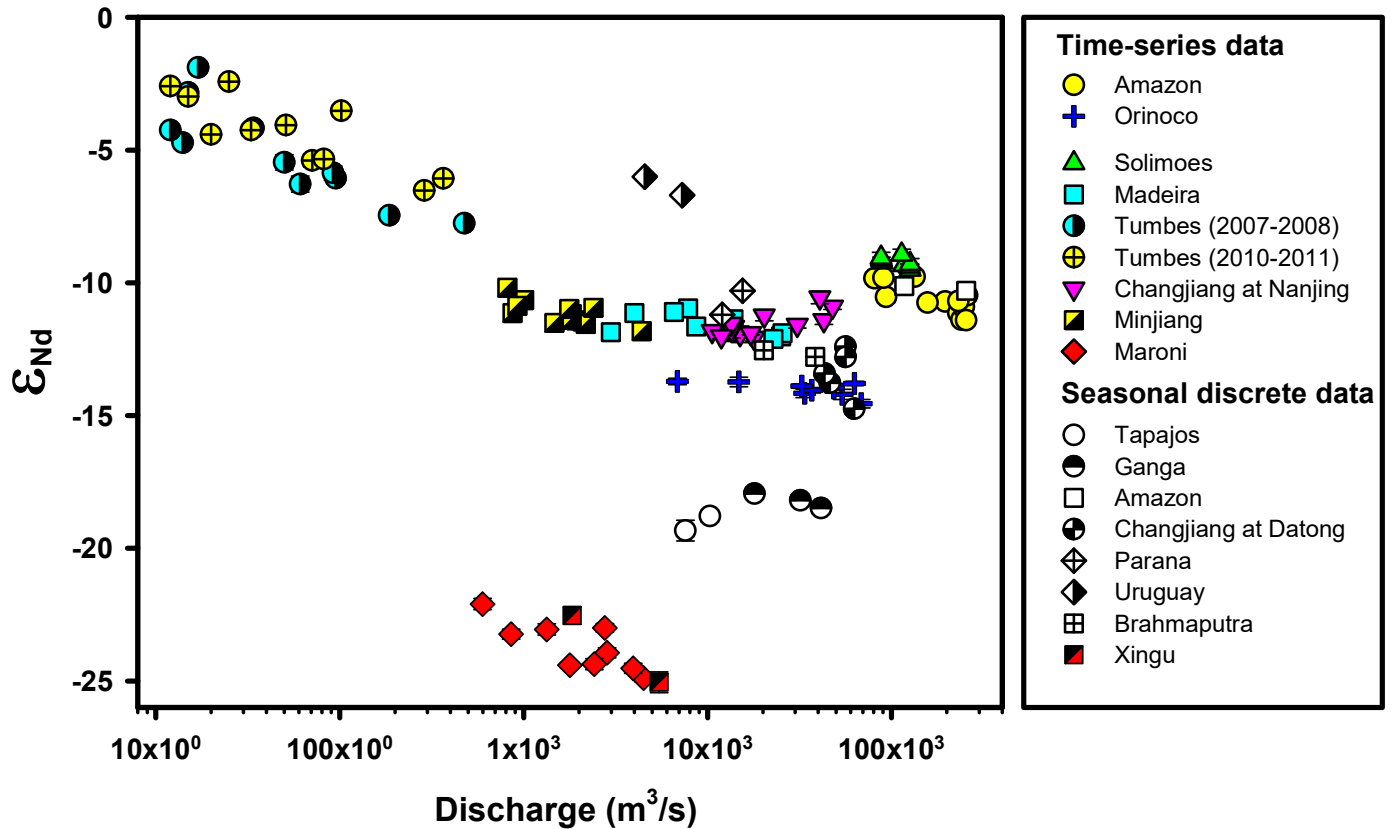


Fig. 5. Dependency of particulate ϵ_{Nd} of global rivers on the solid-solution interaction time, which is regulated by river water discharge. Both the time-series and discrete seasonal data available in literature are plotted. A general decrease of particulate ϵ_{Nd} with water discharge is observed individually for each of the river time-series data evaluated in this study. Parameters of regression analysis for the individual river time-series data are listed in supplementary table ST5. Data sources provided in supplementary table ST4. Note that a global inverse correlation for combined data of all the rivers is neither observed nor anticipated (see text for more details).

1004
 1005
 1006
 1007
 1008
 1009
 1010
 1011
 1012
 1013
 1014
 1015
 1016
 1017
 1018
 1019
 1020
 1021
 1022
 1023
 1024
 1025
 1026
 1027
 1028
 1029
 1030
 1031
 1032
 1033

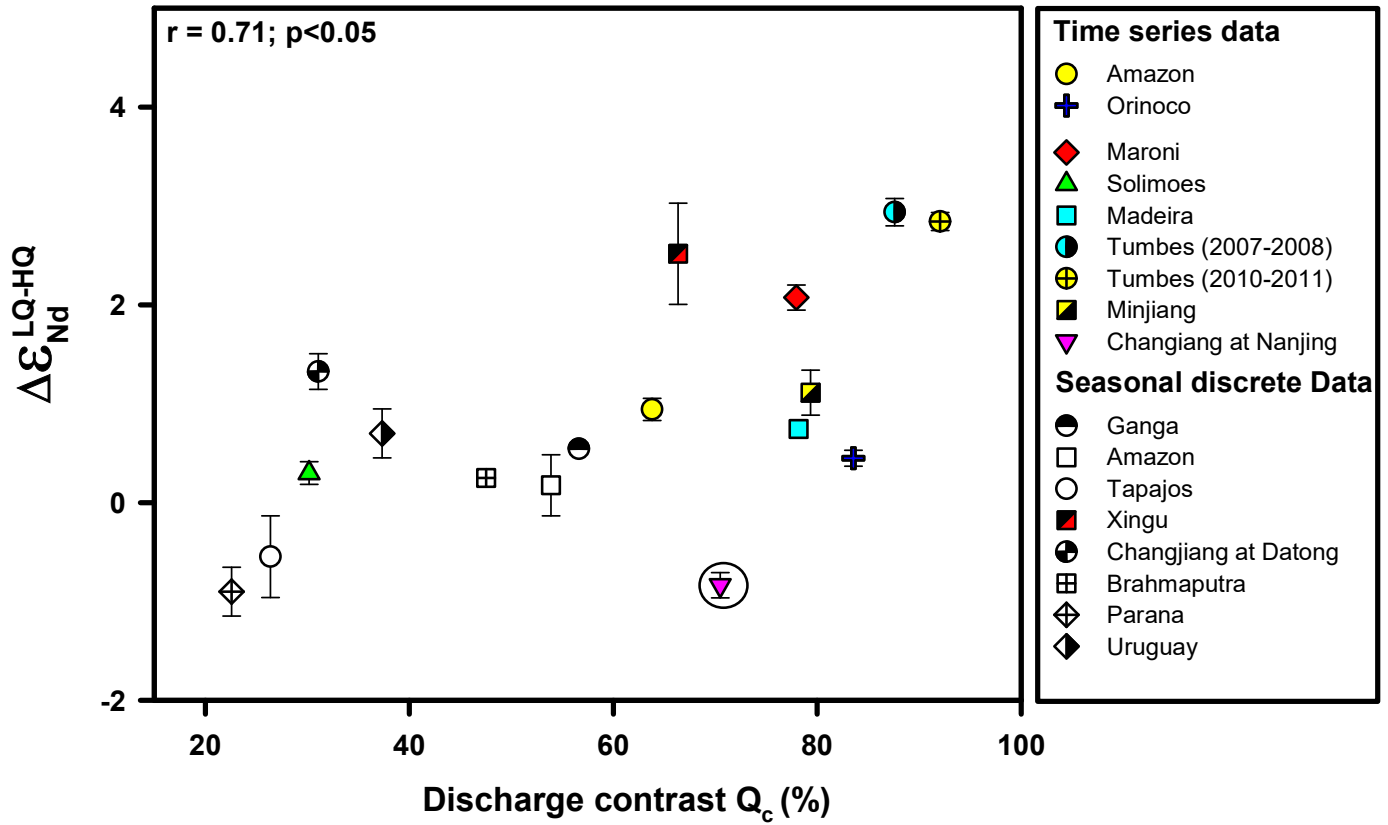


Fig. 6. Impact of seasonal discharge contrast on the difference of particulate ϵ_{Nd} of rivers between low flow and high flow periods. The difference of mean particulate ϵ_{Nd} between low discharge (LQ) and high discharge (HQ) periods scales with the magnitude of discharge contrast (Q_c) between the LQ and HQ periods. Such an observation provides irrefutable evidence for the dominating influence of solid-solution interaction time on the modulation of particulate ϵ_{Nd} of global rivers. Calculations of mean seasonal ϵ_{Nd} and discharge contrast are detailed in supplementary table ST4 and supplementary note SN6. The outlier (circled) of time-series data of the Changjiang River at Nanjing is excluded from regression (see supplementary note SN5 for more details on this dataset).

1034
 1035
 1036
 1037
 1038
 1039
 1040
 1041
 1042
 1043
 1044
 1045
 1046
 1047
 1048
 1049
 1050
 1051
 1052
 1053
 1054
 1055
 1056
 1057
 1058
 1059
 1060

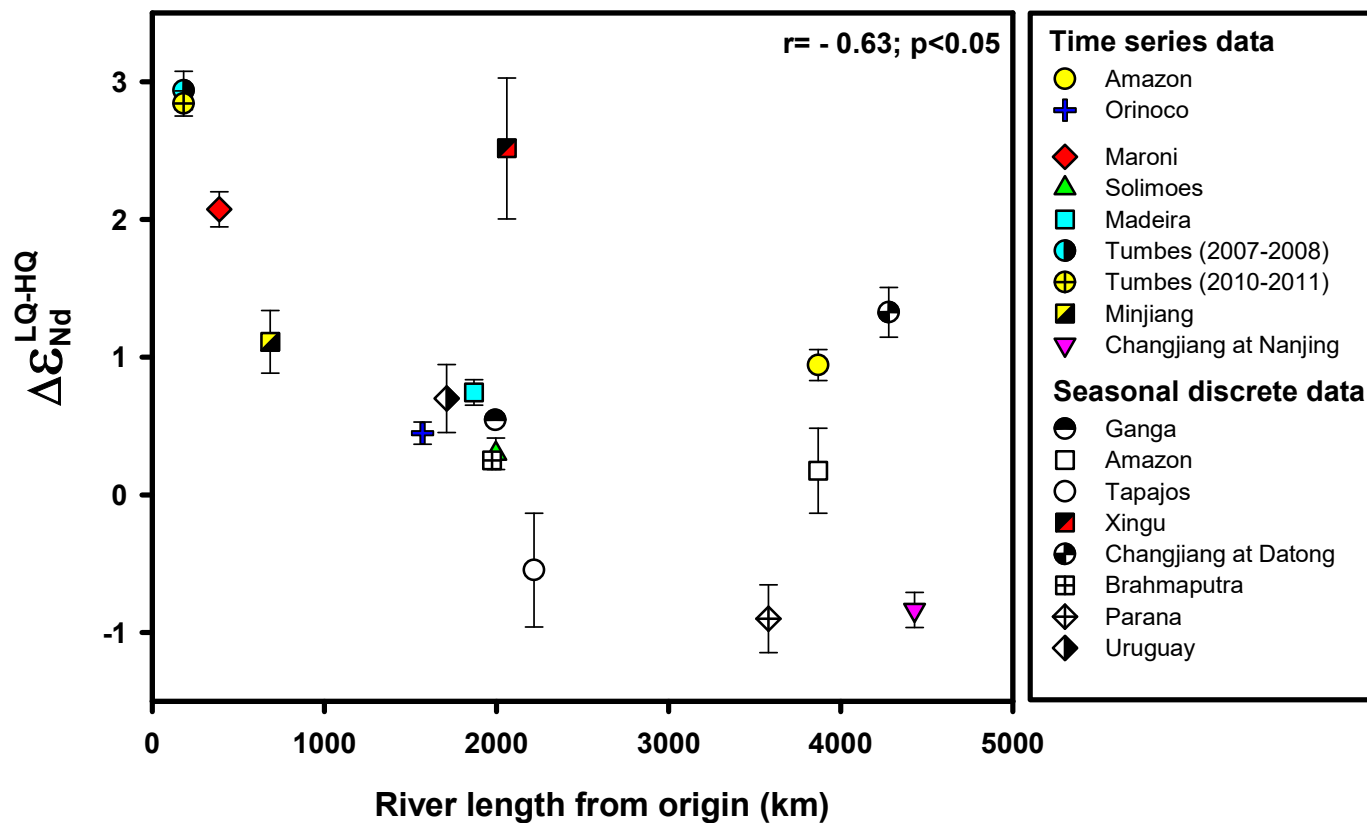
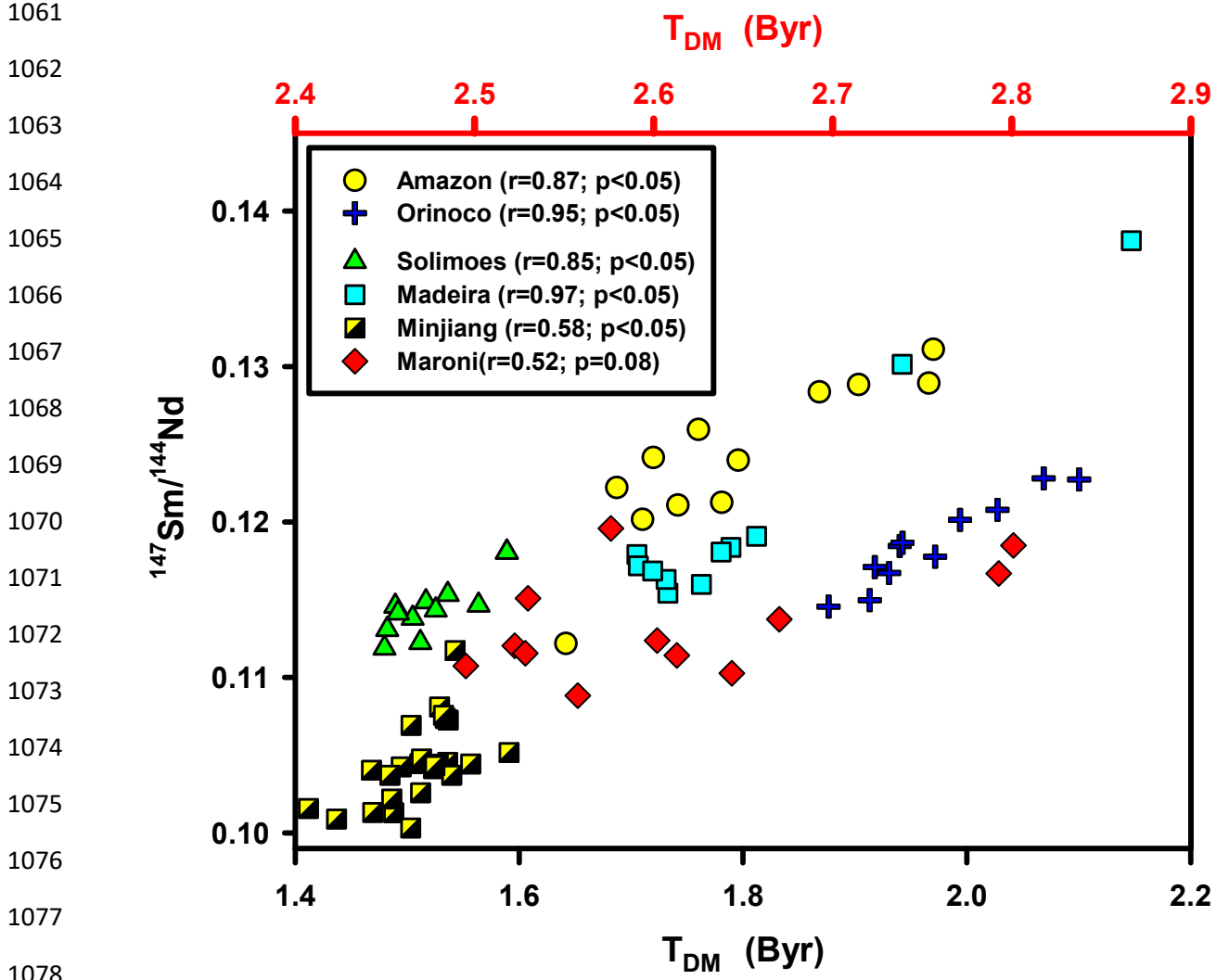


Fig. 7. The influence of transport length on variation of particulate ϵ_{Nd} . The differences of the particulate ϵ_{Nd} between the lean (LQ) and peak (HQ) flow periods demonstrate a generally decreasing trend with length of river transport. Such an observation provides the evidence for modulation of particulate ϵ_{Nd} as a function of length of river transport which influence the adsorption of dissolved Nd via duration of solid-solution interaction. See supplementary table ST4 for the data sources.



1079 **Fig. 8.** Time-series data of river particulate ϵ_{Nd} values are not influenced by age and composition
 1080 of source rocks. The depleted mantle model ages (T_{DM}) of the SPM were determined as $T_{DM} =$

1081
$$\frac{1}{\lambda_{Sm}} \ln \left[\frac{\left(\frac{^{143}Nd}{^{144}Nd}\right)_{sample} - \left(\frac{^{143}Nd}{^{144}Nd}\right)_{DM}}{\left(\frac{^{147}Sm}{^{144}Nd}\right)_{sample} - \left(\frac{^{147}Sm}{^{144}Nd}\right)_{DM}} + 1 \right]$$
 where λ_{Sm} is the decay constant of ^{147}Sm ($6.54 \times 10^{-12} \text{ y}^{-1}$),

1082 $(^{143}Nd/^{144}Nd)_{DM}$ and $(^{147}Sm/^{144}Nd)_{DM}$ of the present day depleted mantle are 0.513155 and
 1083 0.21378, respectively (Goldstein et al., 1984). An inverse correlation is expected if the particulate
 1084 ϵ_{Nd} values are significantly influenced by the model age and composition of source rocks. In
 1085 contrast, significant positive correlations are observed, thus indicating the dominant influence of
 1086 weathering and riverine transport on particulate Sm/Nd and ϵ_{Nd} values. Note that T_{DM} values of
 1087 the Maroni River SPM are plotted against the upper horizontal scale. Data sources: Amazon
 1088 (Rousseau et al., 2019), Orinoco (Rousseau et al., 2019), Maroni (Rousseau et al., 2019),
 1089 Solimoes (Viers et al., 2008), Madeira (Viers et al., 2008) and Minjiang River (Jian et al., 2020a;
 1090 2020b).

1091
1092
1093
1094
1095
1096
1097
1098
1099
1100
1101
1102
1103
1104
1105
1106
1107
1108
1109
1110
1111
1112
1113
1114
1115
1116
1117
1118
1119
1120
1121
1122
1123
1124
1125
1126
1127
1128

Supplementary information for

Incongruent chemical weathering and adsorption of neodymium drive modulation of neodymium isotope composition of global riverine particulate matter

Anup Kumar Sharma¹, Tarun Kumar Dalai¹, Prem Chand Kisku², Jitendra Kumar Pattanaik³, Sambuddha Misra⁴, Shivansh Verma⁵, Anil Dutt Shukla^{5,6}

¹Department of Earth Sciences, Indian Institute of Science Education and Research Kolkata, Mohanpur 741246, India

²Council of Scientific and Industrial Research-National Geophysical Research Institute (CSIR-NGRI), Uppal Road, Hyderabad 500007, India

³Department of Geology, Central University of Punjab, Bathinda, Punjab 151401, India

⁴Centre for Earth Sciences, Indian Institute of Science, Bangalore 560012, India

⁵Geosciences Division, Physical Research Laboratory, Ahmedabad 380009, India

⁶Department of Geology, HNB Garhwal University, Srinagar, Uttarakhand 246174, India

The Supplementary information include:

- 1. Supplementary Note SN1:** The study area.
- 2. Supplementary Note SN2:** Assessment of preservation of weathering profiles and possible aeolian contributions
- 3. Supplementary Note SN3:** Loss of Nd during chemical weathering.
- 4. Supplementary Note SN4:** Determination of ϵ_{Nd} of the residual phases.
- 5. Supplementary Note SN5:** Time-series and seasonal data on global riverine particulate ϵ_{Nd} .
- 6. Supplementary Note SN6:** Averaging of discharge and particulate ϵ_{Nd} of the time-series data
- 7. Supplementary Note SN7:** Modelling the impact of Nd adsorption vis-a-vis ϵ_{Nd} difference between the river water and particulate phase on the seasonal variation of the particulate ϵ_{Nd} .
- 8. Supplementary Figures:** Figure SF1 to Figure SF9.
- 9. Supplementary Table ST1:** Major, trace element and Nd isotope composition of weathering profiles.
- 10. Supplementary Table ST2:** Immobile elemental ratios of parent basalts and weathering profiles.
- 11. Supplementary Table ST3:** The composition of the extracted oxyhydroxide and exchangeable phases. The calculated ϵ_{Nd} values of the residual phases and the ϵ_{Nd} difference between the parent basalt and residual phases are also given.
- 12. Supplementary Table ST4:** Mean particulate ϵ_{Nd} values of global rivers during low and high discharge periods.
- 13. Supplementary Table ST5:** Results of regression analysis of particulate ϵ_{Nd} vs. discharge of time series data.

1129 **Supplementary Note SN1: The Study area**

1130 The Rajmahal Volcanic Province (RVP) covers an area of about 4300 km² and comprises mainly
1131 of basalts and inter-trappean beds (Ghose et al., 2017). The RVP is bounded by the Precambrian
1132 Chotanagpur Gneissic complex (CGS) in the southwest and the Quaternary alluvium of the
1133 Bengal Basin in the east (Supplementary Fig. SF1). The Gondwana Supergroup overlies the CGS
1134 and is underlain by the Rajmahal flood basalts (Ghose et al., 2017).

1135 The Rajmahal basalts have been dated at 118±2 Myr (Ghose et al., 2017). The rocks are
1136 primarily tholeiitic basalts and basaltic andesites, with minor abundance of trachyandesites,
1137 andesites, dacites, and rhyolites. The basalts are made up of labradoritic plagioclase, pigeonitic-
1138 augitic pyroxene, opaque minerals and primary glass (Mukherjee, 1971). The region experiences
1139 today a humid to sub-humid climate, and receives an average annual rainfall of about 1550 mm
1140 mostly via southwest monsoon circulation. Major rivers flowing through the terrain are Gumani,
1141 Brahmani and Bansloi River (Supplementary Fig. SF1).

1142 Two weathering profiles, namely the Dalahi and Pakuria, were collected from the
1143 southern part of the Rajmahal trap in the state of Jharkhand (Supplementary Fig. SF1). The RVP
1144 is characterized by the development of laterites in the eastern part of the province (Ghosh and
1145 Guchhait, 2019). These laterites are characterized by CIA values >99 and are presumed to be of
1146 Eocene-Miocene in age based on presence of the dicotyledonous and angiospermous fossil
1147 woods (Ghosh et al., 2015; Ghosh and Guchhait, 2019). While ferricretes and laterites have been
1148 reported in Pakur district (Ghosh et al., 2015), the concentration of Al is <11 % in both the
1149 profiles, thus clearly indicating that the leaching of the elements are only moderate. Such an
1150 inference is further supported by progressive upward increase of CIA values, with the maximum
1151 values in the range of 75 to 79 in the two studied profiles. We therefore contend that weathering

1152 history of these profiles is much younger, relative to the inferred age of the primary laterites
1153 (Ghosh et al., 2015). The top sample of the Pakuria profile and top two samples of the Dalahi
1154 profile depict abnormal variation trends in the mineralogical and elemental composition (see
1155 [Supplementary Note SN2](#) for a detailed assessment).

1156 The Dalahi profile (DP) is exposed along the southern wall of a stone quarry near the
1157 Dalahi village of Dumka district (24° 13.12' N, 87° 38.76' E; [Supplementary Fig. SF1](#)). At ~50
1158 cm from the surface, ferricrete nodules are observed and traces of these nodules persist up to a
1159 depth of about 90 cm. Saprolites of varying degrees of weathering were observed. Eleven
1160 samples were collected from the upper ~200 cm of the profile. The basalt samples (RJS 12 to 16)
1161 were collected from a ~1.5 m section of an open pit mine situated within ~50 cm of the profile.
1162 The Pakuria profile (PP) is developed near Pakuria village of the Pakur district (24° 18.26' N,
1163 87° 45.30' E; [Supplementary Fig. SF1](#)). This profile was sampled from a well exposed section in
1164 a stone quarry. The total exposed depth of the profile was more than 15 meters. The horizon
1165 within the upper 70 cm was characterized by reddish-brown color and medium to coarse grain
1166 ferricrete nodules. The ongoing weathering is evident from the presence of mixture of saprolites
1167 and mineral fragments between 70 to 625 cm depth of the profile. The top 50 cm was not
1168 sampled to avoid the plant roots and contamination from overburden materials. Nine samples
1169 were collected from the profile. The fresh basalt sample (PFB1) was obtained at a depth of 10
1170 meters.

1171 **Supplementary Note SN2: Assessment of preservation of weathering profiles and possible** 1172 **aeolian contributions**

1173 The preservation and *in-situ* nature of the weathering profile was evaluated using data on major
1174 and trace element compositions ([Supplementary Table ST1](#)). The Si/Al ratios exhibit a general
1175 decrease and the CIA values increase from the parent rock towards the top of the profile, with the

1176 exception of top two samples in DP and the topmost sample in PP ([Supplementary Fig. SF2](#)).
1177 Therefore, elemental compositions clearly document progressive weathering of basaltic rocks,
1178 indicating well preservation of the profiles. The unusual increase of Si/Al ratios in the top two
1179 samples of DP and one sample of PP is presumably due to external influences such as lateral
1180 transport.

1181 The *in-situ* nature and preservation of weathering profiles is routinely assessed by using
1182 immobile element ratios (Maynard, 1992; Nesbitt and Markovics, 1997). The robustness of these
1183 ratios is due to their limited variation during weathering and transport, although their absolute
1184 elemental concentrations could show a considerable scatter. However, the characteristic narrow
1185 range of variation can be violated by mixing with materials external to the weathering profile.
1186 We use two such ratios (Nb/Al and Th/Al) to evaluate the *in-situ* nature of the profiles
1187 ([Supplementary Table ST2, Supplementary Fig. SF2](#)). With the exception of top two samples of
1188 DP and the topmost sample of PP, the mean of the elemental ratios agree within uncertainties
1189 with the ratios measured for the parent basalts. Therefore, the ratios of immobile elemental
1190 concentrations firmly establish the well-preserved and *in-situ* nature of the two profiles. The
1191 trace element ratios of topmost two samples of DP and one sample of PP ([Supplementary Table](#)
1192 [ST2, Supplementary Fig. SF2](#)) are outside the range of the values for the rest of the profile and
1193 the parent rocks. Therefore, based on collective evidence of the mineral, major element and
1194 immobile trace element composition, we infer that the topmost sections (shaded portion in
1195 [Supplementary Fig. SF2](#)) are influenced by lateral transport. Therefore, we exclude data of these
1196 samples from further evaluation and discussion.

1197 The excellent agreement of the immobile element ratios between the parent basalts and
1198 weathering profile samples also indicates the aeolian contributions to be insignificant. We

1199 corroborate such an assessment through three immobile elements (La-Th-Sc) discrimination
 1200 diagram that is routinely employed to determine source compositions (Wang et al., 2018; Yuan et
 1201 al., 2022). It is evident ([Supplementary Fig. SF3](#)) that the immobile element compositions of the
 1202 weathering profiles are distinctly different than those of the potential dust sources, but nearly
 1203 identical to those of the parent basalts. These observations confirm our contention that the two
 1204 studied profiles are not contaminated by aeolian contributions.

1205 **Supplementary Note SN3: Loss of Nd during chemical weathering**

1206 The percentage loss of Nd from the weathering profiles were determined as follows:

1207
$$[Nd]_{lost} \% = \left[1 - \left(\frac{[Nd]_{bulk}}{[Nd]_p} \right) \right] \times 100 \quad \text{Eq. (1)}$$

1208 where subscripts *bulk* and *P* refer to the [Nd] in the bulk weathered materials and parent basalts,
 1209 respectively. Th is used as a normalizing element due to its immobile behavior during the
 1210 chemical weathering of basalts (Ma et al., 2007).

1211 **Supplementary Note SN4: Determination of ϵ_{Nd} of the residual phases**

1212 The ϵ_{Nd} values of the residual phases were calculated based on the premise that the bulk materials
 1213 of the profiles are composed of the residual products and components adsorbed from the
 1214 weathering solutions onto the oxyhydroxide phases. The ϵ_{Nd} of the adsorbed components was
 1215 considered to be the same as measured on oxyhydroxides phases. Mass balance relations for the
 1216 Nd and ϵ_{Nd} are:

1217
$$f_{Nd}^{Res} = 1 - \left(\frac{[Nd]_{ads}}{[Nd]_{bulk}} \right) = 1 - \left(\frac{[Nd]_{ox}}{[Nd]_{bulk}} \right) \quad \text{Eq. (2)}$$

1218
$$f_{Nd}^{ox} = \frac{[Nd]_{ox}}{[Nd]_{bulk}} \quad \text{Eq. (3)}$$

1219
$$\varepsilon_{Nd}^{bulk} = f_{Nd}^{Res} \times \varepsilon_{Nd}^{Res} + f_{Nd}^{ox} \times \varepsilon_{Nd}^{ox} \quad \text{Eq. (4)}$$

1220 where f_{Nd} denotes the fraction of Nd in the bulk phase, and the terms *ads*, *Res* and *ox*
 1221 refer to residual and oxyhydroxides, respectively. The ε_{Nd} values of adsorbed and residual
 1222 component are calculated as:

1223
$$\varepsilon_{Nd}^{ads} = \varepsilon_{Nd}^{ox} \quad \text{Eq. (5)}$$

1224
$$\varepsilon_{Nd}^{Res} = \left(\frac{\varepsilon_{Nd}^{bulk} - [f_{Nd}^{ox} \times \varepsilon_{Nd}^{ox}]}{f_{Nd}^{Res}} \right) \quad \text{Eq. (6)}$$

1225 The values of ε_{Nd}^{ox} and ε_{Nd}^{Res} are listed in supplementary Table ST3.

1226 **Supplementary Note SN5: Time-series and seasonal data on global riverine particulate ε_{Nd}**

1227 The time-series data of rivers evaluated in this study are from existing literature and cover at
 1228 least one full annual discharge cycle for Amazon, Orinoco, Madeira, Solimoes, Maroni, Tumbes,
 1229 Minjiang and Changjiang ([Supplementary Table ST4](#)). The discrete seasonal ε_{Nd} data represent
 1230 the dry and wet periods for the rivers Ganga, Brahmaputra, Amazon, Changjiang, Uruguay,
 1231 Tapajos, Parana, and Xingu. However, these data do not represent the maximum and minimum
 1232 flow conditions of an annual discharge cycle. The discharge (Q) and SPM concentration data for
 1233 the Minjiang River (Jian et al., 2020b) were obtained from figures using PlotDigitizer software
 1234 that has been reported to extract data reliably (Aydin and Yassikaya, 2021).

1235 With the exception of the Changjiang data at Nanjing, eight sets of time-series data
 1236 representing seven rivers individually demonstrate clear inverse ε_{Nd} -Q relationships
 1237 ([Supplementary Table ST5](#)). The ε_{Nd} data of the Changjiang River SPM were measured after
 1238 leaching the bulk SPM with 0.5 M acetic acid (Mao et al., 2011) The amorphous Fe-Mn
 1239 oxyhydroxides are soluble, albeit sparingly, in acetic acid (Tachambalath et al., 2023). Therefore,
 1240 it is unclear how and to what degree Nd hosted by amorphous oxyhydroxides may have been

1241 impacted by acid leaching. Furthermore, after the construction of the Three Gorges Dam,
1242 increased channel erosion in the lower reaches has been reported to contribute more
1243 unradiogenic Nd in the dry seasons (Mao et al., 2011). Although the variation of ϵ_{Nd} with
1244 discharge has been explained in terms of variable contributions of sediments from upper and
1245 lower reaches of river (Mao et al., 2011), the lack of data on [Nd] does not allow us to test if
1246 mixing is responsible for the observed ϵ_{Nd} -Q relationship. The idea that the dissolved phase of
1247 this river could have been less radiogenic than the SPM is not supported by the discrete seasonal
1248 data available at Datong (Luo et al., 2012) which show a higher particulate ϵ_{Nd} in the low
1249 discharge period ([Supplementary Table ST4](#)). We therefore contend that further studies of time-
1250 series data of coexisting dissolved-SPM phases both the in the upper and lower reaches are
1251 required for a reliable evaluation of the processes regulating the seasonal variation of particulate
1252 ϵ_{Nd} of the Changjiang River.

1253 In the discrete-seasonal datasets, six of the eight rivers are characterized by higher
1254 particulate ϵ_{Nd} in the low discharge periods, which is supportive of our framework of
1255 interpretation. While the discrete low-resolution data could be biased by unusual and extreme
1256 fluctuations, the following circumstantial evidence supports the seasonal trend of particulate ϵ_{Nd}
1257 data for the Ganga and Brahmaputra Rivers. The dissolved phase of the Ganga River has been
1258 reported to have higher ϵ_{Nd} than the coexisting SPM (Chatterjee and Singh, 2014). In addition,
1259 the study of Galy et al. (1998) reported that the clay fractions of the Ganga and Brahmaputra
1260 rivers, bearing a greater potential for Nd adsorption, have ϵ_{Nd} values up to 3 units higher than the
1261 bedload samples.

1262 The discrete seasonal data of three rivers (Amazon, Tapajos and Xingu) are characterized
1263 by low precision for the particulate ϵ_{Nd} ($\pm 2\sigma = 0.14$ to 0.39). Out of these, one river shows

1264 negative values of $\Delta\epsilon_{Nd}^{LQ-HQ}$. However, owing to large uncertainties, the $\Delta\epsilon_{Nd}^{LQ-HQ}$ values are
1265 indistinguishable from zero.

1266 **Supplementary Note SN6: Averaging of discharge and particulate ϵ_{Nd} of the time-series**
1267 **data**

1268 In order to minimize the bias due to extreme fluctuations, the seasonal averaging of discharge
1269 and ϵ_{Nd} of the time-series data were performed after excluding the distinct outliers
1270 (Supplementary Table ST4). The scheme of data averaging depended on the discharge contrast
1271 between seasons and temporal resolution of available ϵ_{Nd} data in a given flow period. Such a
1272 scheme involved averaging data of samples representing ~35% and ~15% of the lowest and
1273 highest discharge, respectively. Two to six data points were used to calculate the means for both
1274 the low and high flow periods (ϵ_{Nd}^{LQ} and ϵ_{Nd}^{HQ}). However, for the river Minjiang, no averaging could
1275 be done for the high flow period due to lack of enough ϵ_{Nd} data. The errors of average ϵ_{Nd} values
1276 (Supplementary Table ST4) are determined from the reported uncertainties in the literature.

1277 **Supplementary Note SN7: Modelling the impact of Nd adsorption vis-a-vis ϵ_{Nd} difference**
1278 **between the river water and particulate phase on the seasonal variation of the particulate**
1279 **ϵ_{Nd}**

1280 We utilized a mass balance model to elucidate the impact of adsorption on ϵ_{Nd} of SPM during
1281 peak and lean flow periods. The model was constructed based on the assumption that prior to Nd
1282 adsorption in rivers, ϵ_{Nd} of SPM (ϵ_{Nd}^{SPMo}), and ϵ_{Nd} of the river water (ϵ_{Nd}^{Riv}) are the same during the
1283 peak and lean flow periods.

1284 For the peak flow period:

$$1285 \quad \epsilon_{Nd}^{HQ} = f_{Nd}^{HQ} \times \epsilon_{Nd}^{Riv} + (1 - f_{Nd}^{HQ}) \times \epsilon_{Nd}^{SPMo} \quad \text{Eq. (7)}$$

1286 For the lean flow period:

1287
$$\varepsilon_{Nd}^{LQ} = f_{Nd}^{LQ} \times \varepsilon_{Nd}^{Riv} + (1 - f_{Nd}^{LQ}) \times \varepsilon_{Nd}^{SPM_o}$$
 Eq. (8)

1288 where f_{Nd} denotes the fraction of Nd adsorbed onto the riverine SPM, and ε_{Nd}^{HQ} and ε_{Nd}^{LQ} represent
 1289 the Nd isotopic composition of the riverine SPM after Nd adsorption during the high flow and
 1290 low flow periods, respectively.

1291 From eq. (7) and (8), we get

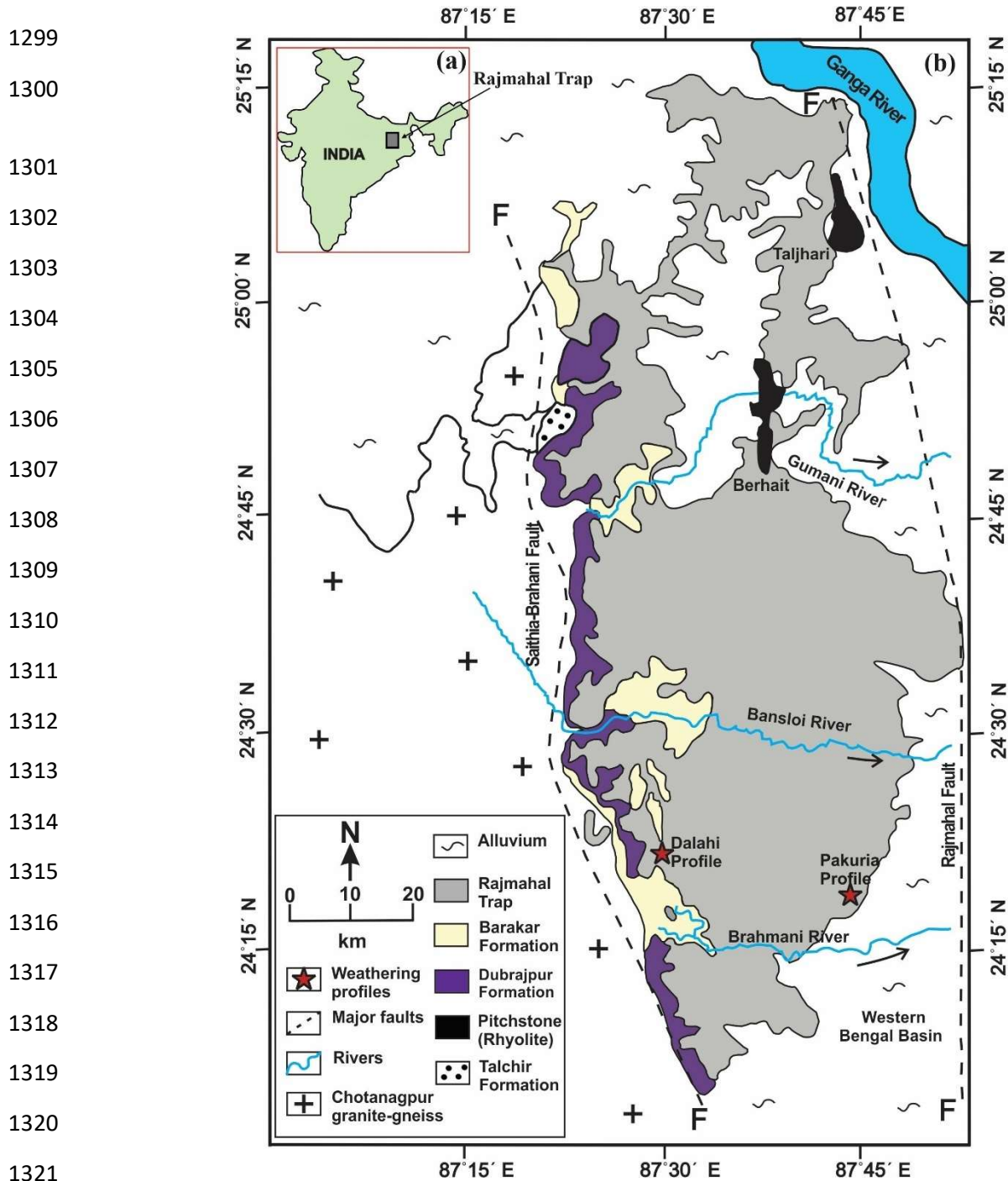
1292
$$(\varepsilon_{Nd}^{LQ} - \varepsilon_{Nd}^{HQ}) = (f_{Nd}^{LQ} - f_{Nd}^{HQ}) \times (\varepsilon_{Nd}^{Riv} - \varepsilon_{Nd}^{SPM_o})$$
 Eq. (9)

1293 Therefore,

1294
$$\Delta\varepsilon_{Nd}^{LQ-HQ} = \Delta f_{Nd}^{LQ-HQ} \times \Delta\varepsilon_{Nd}^{Riv-SPM_o}$$
 Eq. (10)

1295 The expression (Eq. 10) clearly demonstrates that seasonal difference of adsorbed Nd fractions
 1296 and ε_{Nd} difference between the river water and SPM prior to adsorption, together influence
 1297 $\Delta\varepsilon_{Nd}^{LQ-HQ}$ (cf. [Supplementary Fig. SF4](#)).

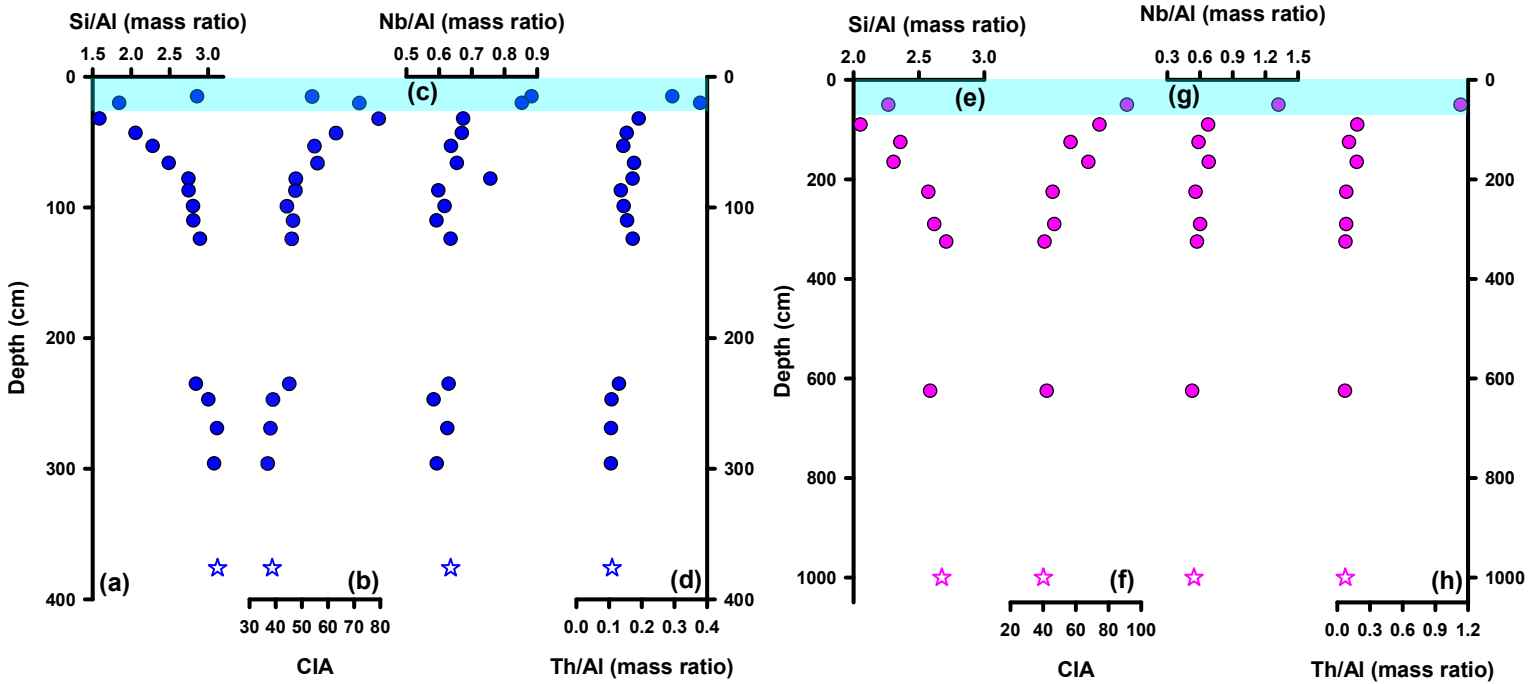
1298



1323 **Supplementary Fig. SF1.** The study area and weathering profiles. (a) The trap basalts of the Rajmahal
 1324 Volcanic Province in India. (b) Geological map of the Rajmahal Volcanic Province (modified after Ghose
 1325 et al. 2017), showing the areal extent of trap basalts and location of the studied weathering profiles (red
 1326 stars). The formations of the Gondwana Supergroup (Dubrajpur, Barakar and Talchir formations) and
 1327 Chotanagpur granite-gneiss are also shown.

1328

1329
1330
1331
1332

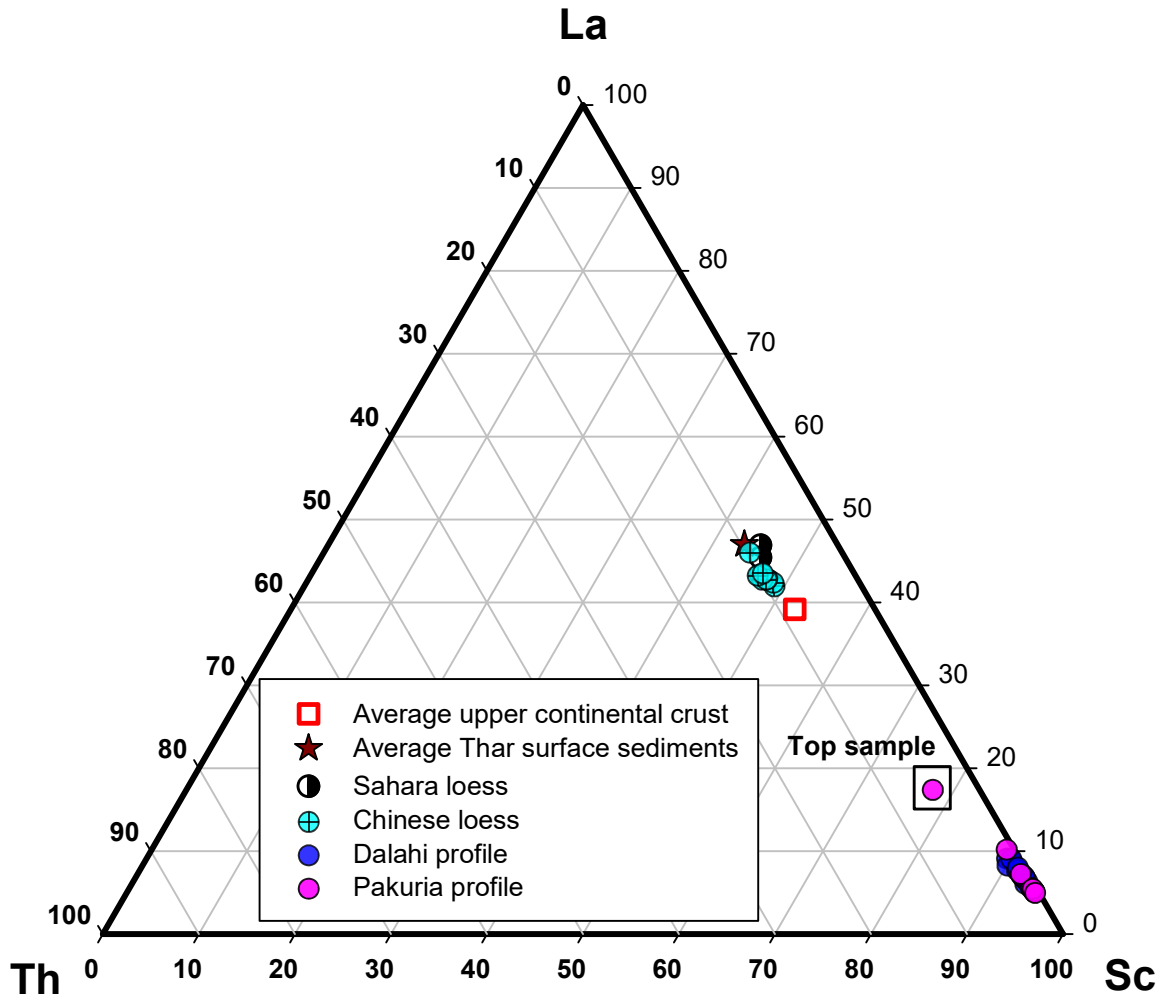


1344
1345

1346 **Supplementary Fig. SF2.** Progressive weathering and preservation of weathering profiles. **(a, b, e, f):**
1347 Upward decrease of Si/Al and increase of CIA indicate progressive weathering towards the top. **(c, d, g,**
1348 **h):** Variation of immobile element ratios (Nb/Al and Th/Al) in the weathered-materials and parent basalts
1349 (stars). Comparable ratios between the parent basalts and the weathered-materials attest to the *in-situ*
1350 characteristics of the profiles. The shaded top portions are inferred to be contaminated by lateral transport,
1351 as evident from Nb/Al and Th/Al ratios that are very different compared to parent basalts (See
1352 [Supplementary Note SN2](#) for the detailed discussion). Dalahi profile: blue, Pakuria profile: pink.

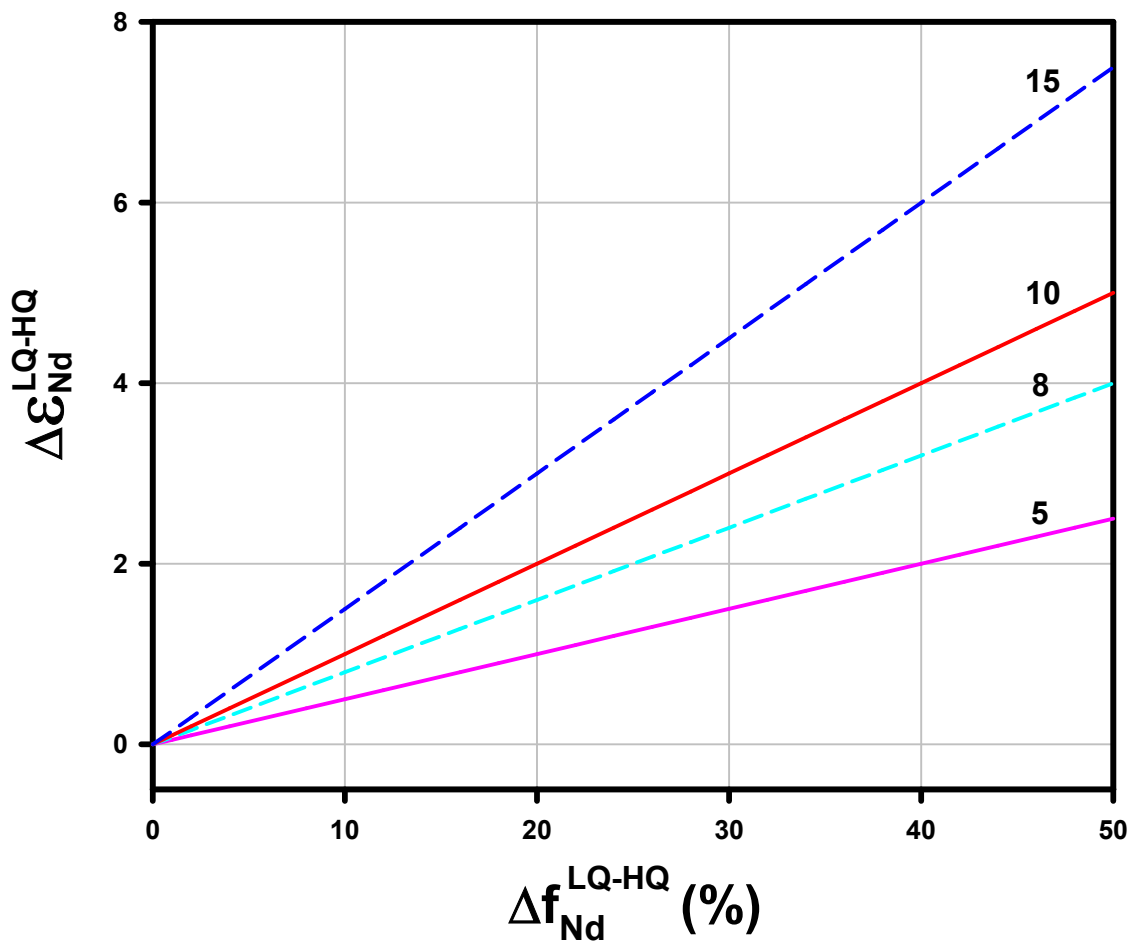
1353
1354
1355
1356
1357
1358
1359
1360

1361
1362
1363
1364
1365
1366
1367
1368
1369
1370
1371
1372
1373
1374
1375
1376
1377
1378
1379
1380
1381
1382
1383
1384
1385
1386
1387
1388
1389
1390
1391



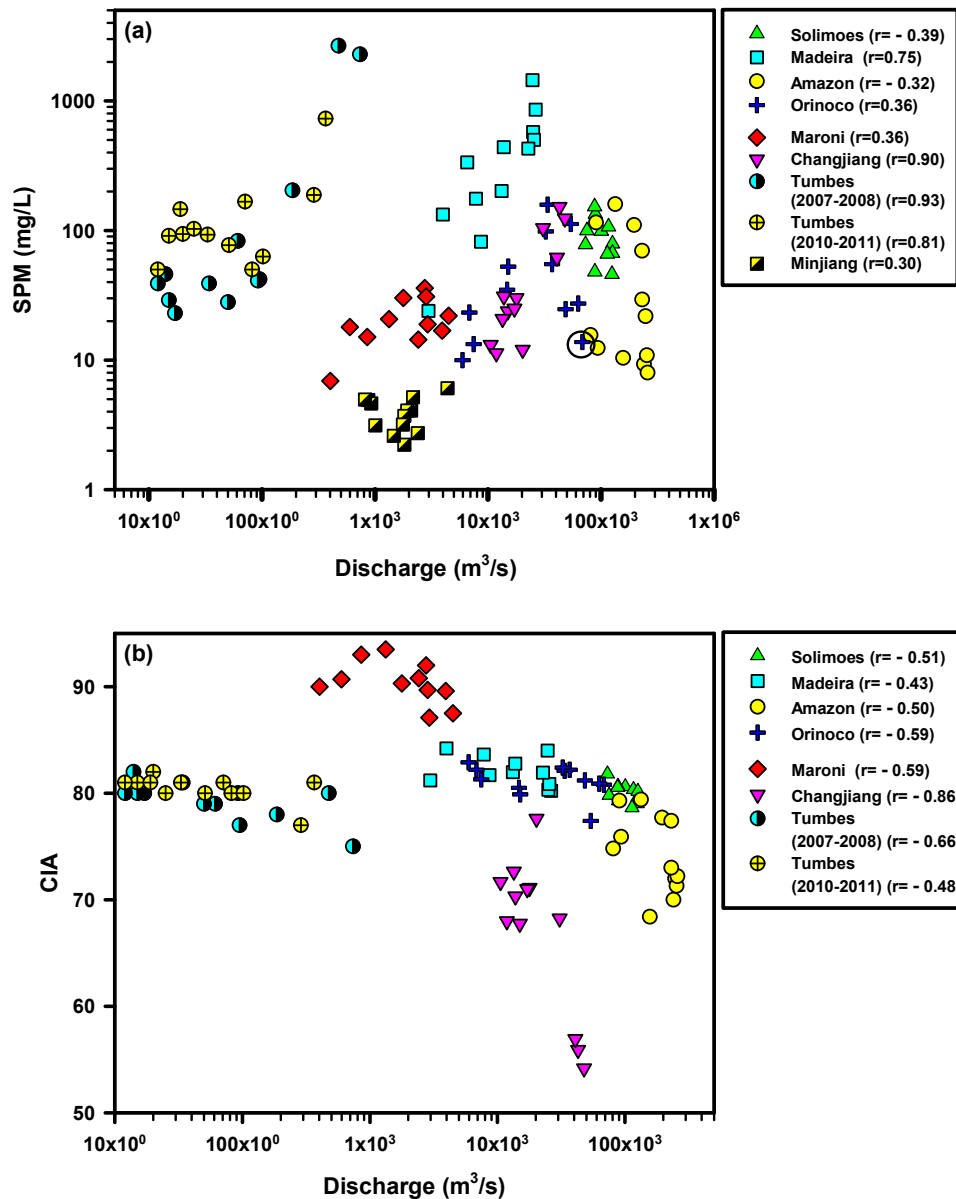
Supplementary Fig. SF3. The La–Th–Sc discrimination diagram comparing the distributions of immobile elements in the two basaltic weathering profiles (including the parent basalts) with those in the average upper continental crust (Taylor and McLennan, 1985), and the primary sources of aeolian dust in Asia: Thar desert surface sample (Bhattacharyya et al., 2024), and loess from China (Wang et al., 2018) and the Sahara (Chauvel et al., 2014). The weathering profile samples have distinctly different compositions compared to the potential dust sources. The concentrations data for the weathering profiles are given in supplementary table ST1.

1392
 1393
 1394
 1395
 1396
 1397
 1398
 1399
 1400
 1401
 1402
 1403
 1404
 1405
 1406
 1407
 1408
 1409
 1410
 1411
 1412
 1413
 1414
 1415
 1416
 1417
 1418
 1419
 1420



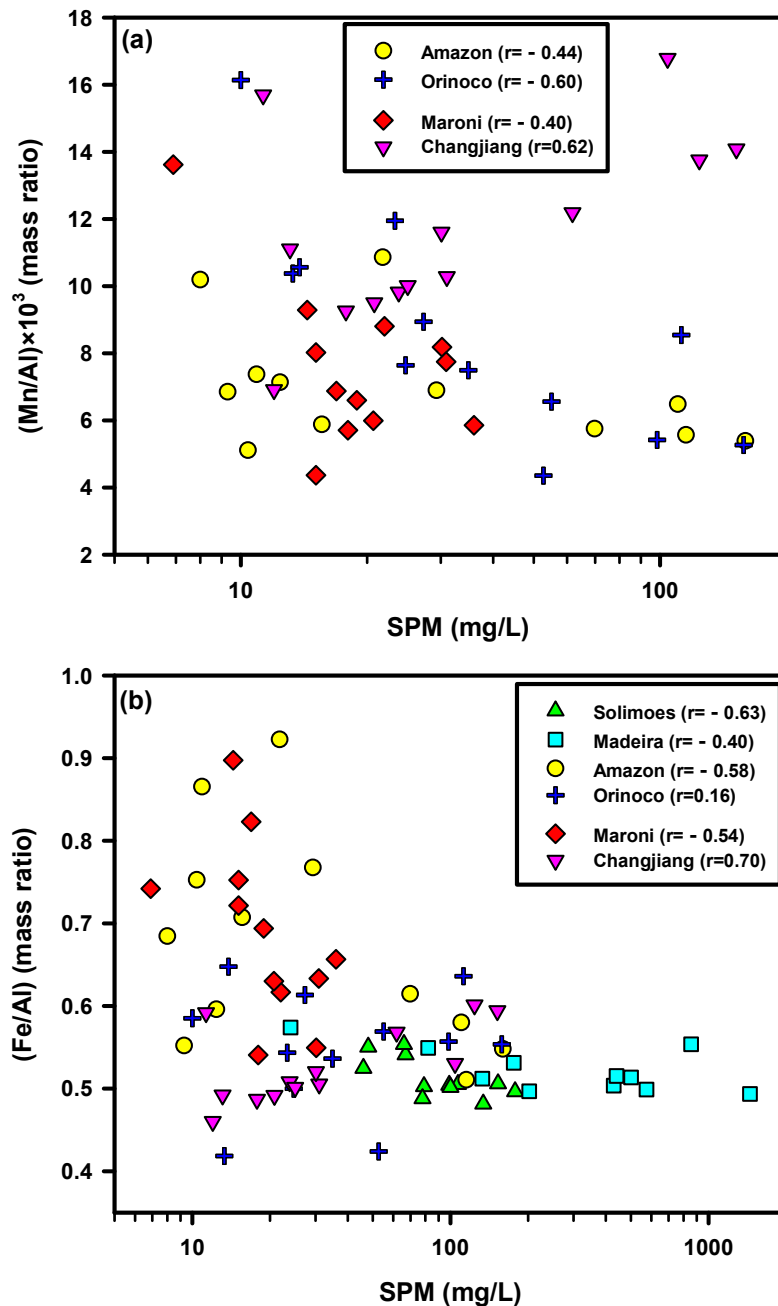
Supplementary Fig. SF4. Combined impact of Nd adsorption and $\Delta \epsilon_{Nd}^{Riv-SPM_o}$ on $\Delta \epsilon_{Nd}^{LQ-HQ}$. Variation of $\Delta \epsilon_{Nd}^{LQ-HQ}$ as a function of difference in the degree of Nd adsorption and difference of ϵ_{Nd} between dissolved phase and SPM. The lines correspond to variable values of $\Delta \epsilon_{Nd}^{Riv-SPM_o}$. The choice of $\Delta \epsilon_{Nd}^{Riv-SPM_o}$ were based on the reported $\Delta \epsilon_{Nd}^{Riv-SPM}$ of ~5 (Hindshaw et al., 2018b) and ~8 (Larkin et al., 2021), $\Delta \epsilon_{Nd}^{Leach-Residu}$ of ~4 (Tricca et al., 1999) and 15 (Hindshaw et al., 2018a). See Supplementary Note SN7 for the mass balance model developed to elucidate the influence of Δf_{Nd}^{LQ-H} and $\Delta \epsilon_{Nd}^{Riv-SPM_o}$ on $\Delta \epsilon_{Nd}^{LQ-HQ}$.

1421
 1422
 1423
 1424
 1425
 1426
 1427
 1428
 1429
 1430
 1431
 1432
 1433
 1434
 1435
 1436
 1437
 1438
 1439
 1440
 1441
 1442
 1443
 1444
 1445
 1446
 1447
 1448
 1449
 1450
 1451



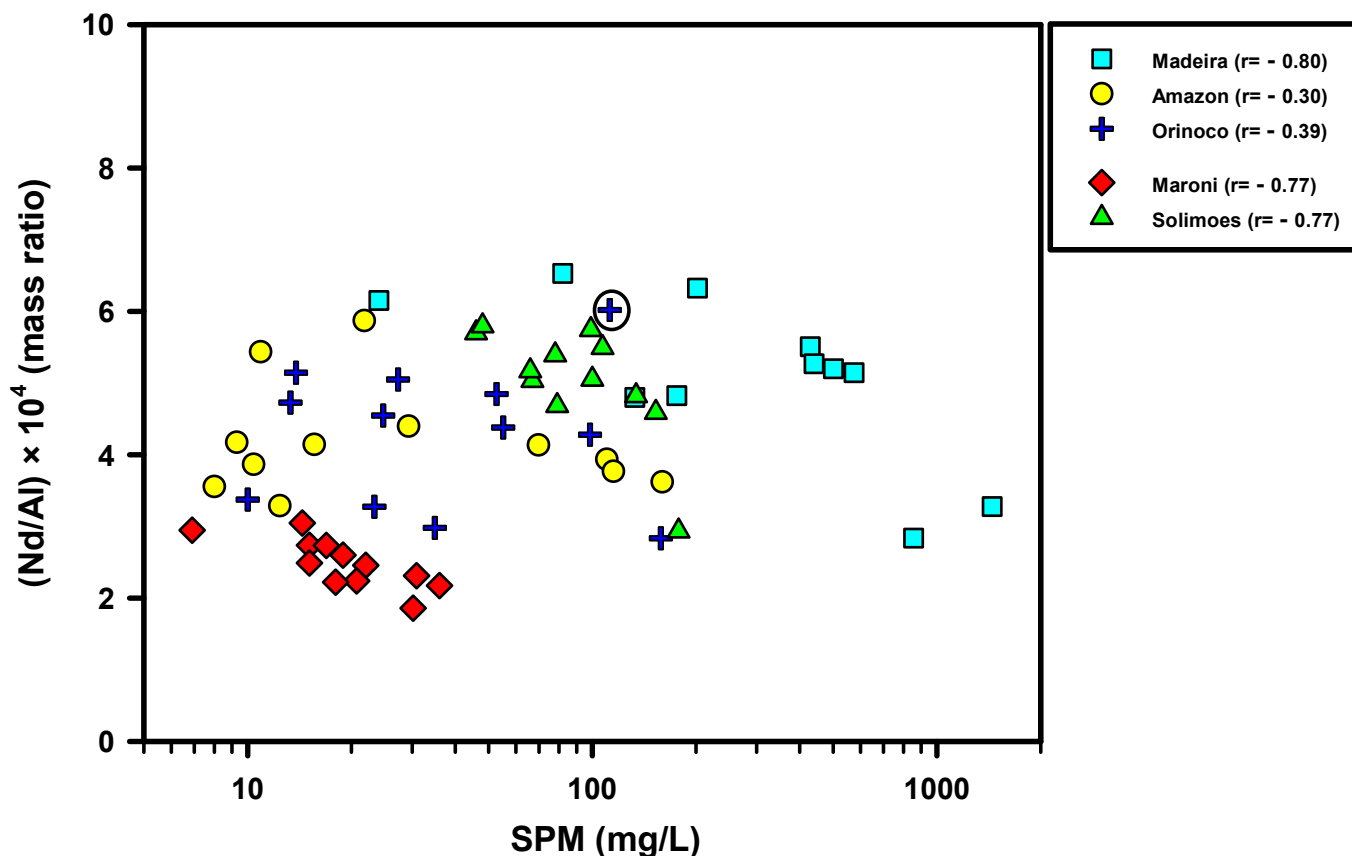
Supplementary Fig. SF5. Variation of [SPM] **(a)** and chemical index of alteration (CIA) **(b)** as a function of river water discharge. **(a)** SPM concentrations are typically higher in the high discharge periods with the exception of the Amazon and Solimoes Rivers, which show the least variation in discharge (Supplementary Table ST4). **(b)** General inverse correlations between CIA and river water discharge indicate a higher degree of chemical weathering and production of secondary minerals in the low flow periods due to longer solid-solution contact time. One outlier (circled) is excluded from regression analysis. Data sources: Amazon (Rousseau et al., 2019), Orinoco (Rousseau et al., 2019), Maroni (Rousseau et al., 2019), Solimoes (Viers et al., 2008), Madeira (Viers et al., 2008), Minjiang (Jian et al., 2020a; 2020b), Tumbes (Moquet et al., 2020) and Changjiang River (Mao et al., 2010). CIA values of the Changjiang River were calculated using major element oxides data sourced from Mao et al. (2010).

1452
 1453
 1454
 1455
 1456
 1457
 1458
 1459
 1460
 1461
 1462
 1463
 1464
 1465
 1466
 1467
 1468
 1469
 1470
 1471
 1472
 1473



1474 **Supplementary Fig. SF6.** Abundance of oxyhydroxide phases as a function of SPM concentrations.
 1475 Inverse correlations of Fe/Al and Mn/Al ratios with SPM concentrations are apparent for all rivers except
 1476 the Changjiang River. For Orinoco River, no significant correlation is observed between Fe/Al and SPM
 1477 concentrations. The observations of this figure and Supplementary Fig. SF5 together indicate higher
 1478 abundances of oxyhydroxide phases (adsorbents) in the low flow periods. Data sources: Amazon
 1479 (Rousseau et al., 2019), Orinoco (Rousseau et al., 2019), Maroni (Rousseau et al., 2019), Solimoes (Viers
 1480 et al., 2008), Madeira (Viers et al., 2008) and Changjiang River (Mao et al., 2010).

1481
1482
1483
1484
1485
1486
1487
1488
1489
1490
1491
1492
1493
1494
1495
1496
1497
1498
1499
1500
1501
1502
1503
1504
1505



Supplementary Fig. SF7. Nd adsorption as a function of SPM concentrations. General inverse correlations of Nd/Al ratio with SPM concentrations indicate higher degree of Nd adsorption at lower SPM concentrations, which is observed in low flow periods when the oxyhydroxide phase concentrations are relatively higher (cf. [Supplementary Fig. SF5-6](#)). One Outlier (circled) is excluded from regression analysis. Data sources: Amazon (Rousseau et al., 2019), Orinoco (Rousseau et al., 2019), Maroni (Rousseau et al., 2019), Solimoes (Viers et al., 2008) and Madeira River (Viers et al., 2008).

1506

1507

1508

1509

1510

1511

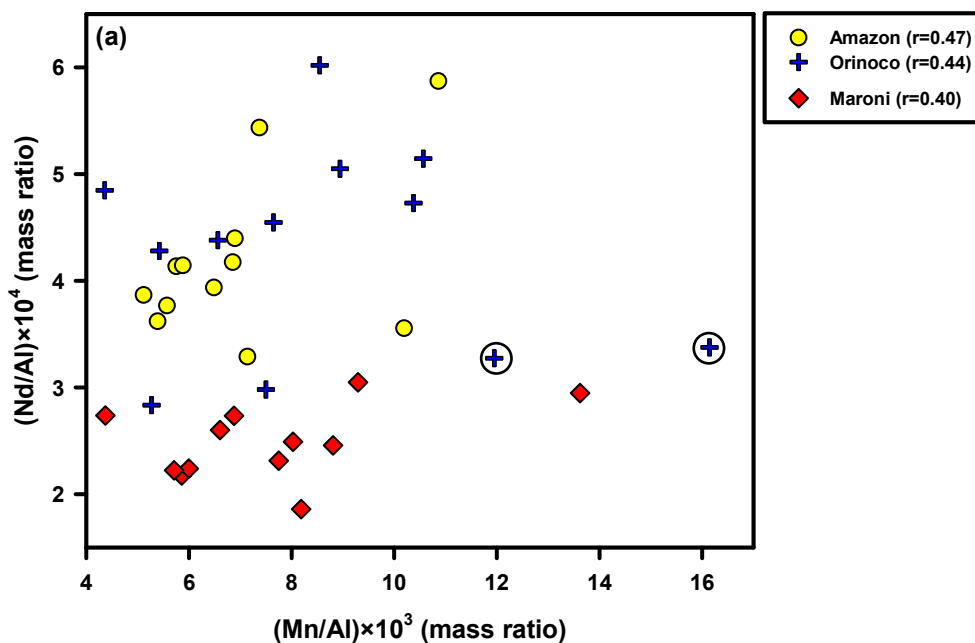
1512

1513

1514

1515

1516



1517

1518

1519

1520

1521

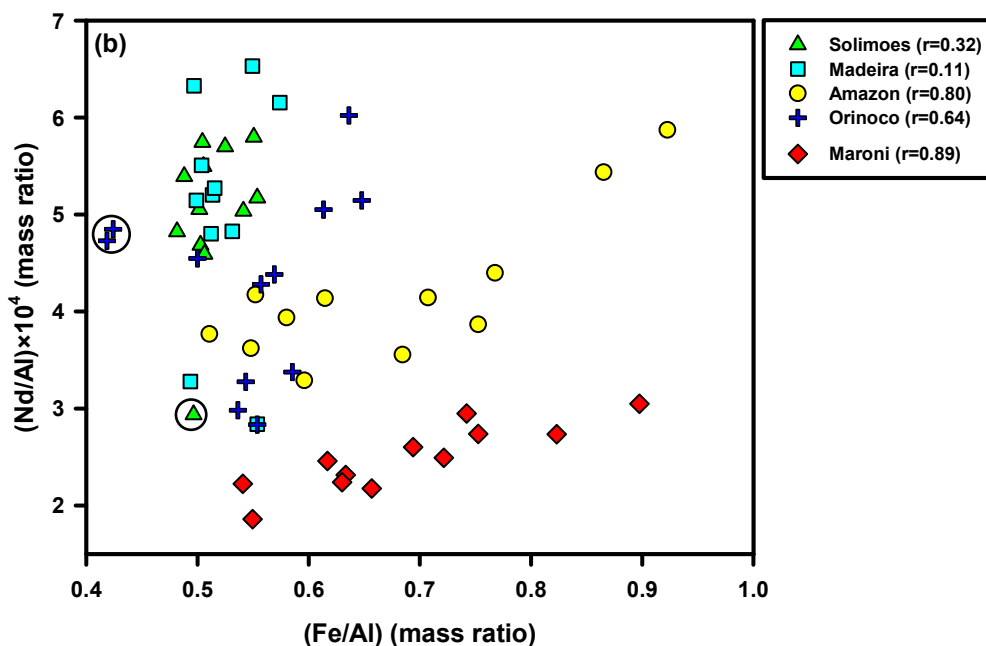
1522

1523

1524

1525

1526



1527

1528

1529

1530

1531

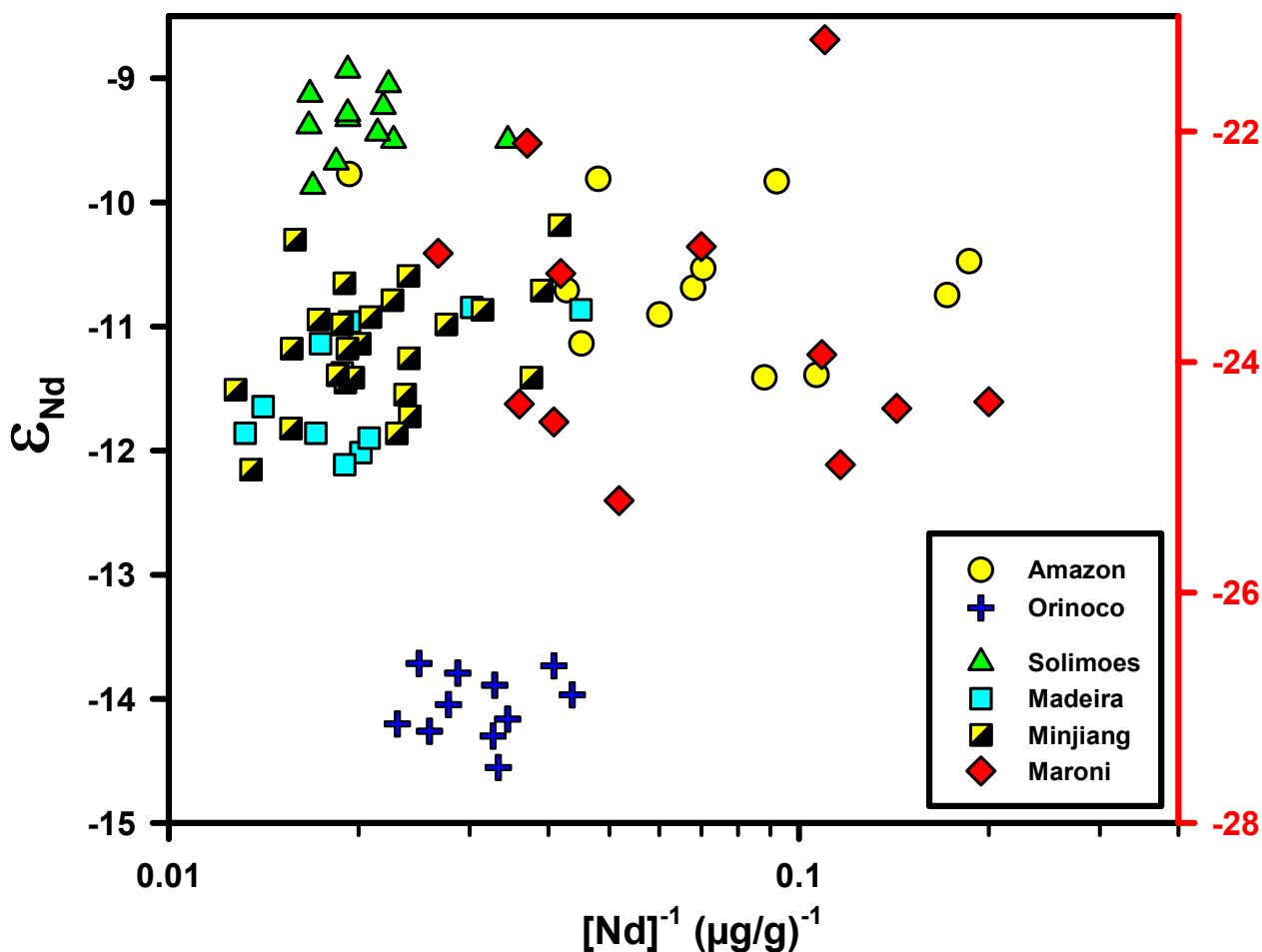
1532

1533

1534

Supplementary Fig. SF8. Nd adsorption as function of abundance of [Fe]-[Mn] oxyhydroxide phases in the SPM. Variation of Nd/Al with the Mn/Al (a) and Fe/Al (b) in the river SPM. Weak to significant positive correlations are observed. The observed variation trends are suggestive of a greater degree of Nd adsorption at higher concentrations of oxyhydroxide phases in the river SPM. Outliers (circled) are excluded from regression analysis. Data sources: Amazon (Rousseau et al., 2019), Orinoco (Rousseau et al., 2019), Maroni (Rousseau et al., 2019), Solimoes (Viers et al., 2008) and Madeira River (Viers et al., 2008).

1535
1536
1537
1538
1539
1540
1541
1542
1543
1544
1545
1546
1547
1548
1549
1550
1551
1552
1553
1554
1555



1556 **Supplementary Fig. SF9.** Evaluation of mixing of source rock contributions to the time-series particulate
1557 ϵ_{Nd} data. Large scatter in the data and a lack of significant linear correlation do not support mixing of
1558 variable source rock composition as a driving process for the temporal variation of particulate ϵ_{Nd} of the
1559 global rivers. Note that ϵ_{Nd} values for Maroni River are plotted against the right-hand side vertical scale.
1560 Data sources: Amazon (Rousseau et al., 2019), Orinoco (Rousseau et al., 2019), Maroni (Rousseau et al.,
1561 2019), Solimoes (Viers et al., 2008), Madeira (Viers et al., 2008) and Minjiang River (Jian et al., 2020a;
1562 2020b).

1563

Supplementary Table ST1. Major, trace element and Nd isotope composition of weathering profiles.

Sample code	Depth (cm)	Al	Ca	Fe	Mg	Na	K	Si	Mn	CIA*	Nb	Nd	Sm	Sc	La	Th	$\epsilon_{Nd}^{\#}$
		wt. %									$\mu\text{g/g}$						
Dalahi profile (DP)																	
RJS 1	15	8.25	4.15	10.2	2.27	1.10	0.26	23.6	0.23	54	7.28	17.7	4.70	35.2	11.3	2.42	NA
RJS 2	20	10.2	2.29	12.8	1.48	0.65	0.17	18.7	0.31	72	8.66	21.7	4.50	43.3	12.6	3.85	NA
RJS 3	32	11.2	1.63	14.3	0.96	0.55	0.12	17.8	0.35	79	7.55	21.3	4.52	48.7	10.2	2.14	-1.12
RJS 4	43	9.97	3.40	12.5	1.96	1.01	0.12	20.5	0.35	63	6.67	19.8	4.85	43.6	10.2	1.54	-0.49
RJS 5	53	9.53	4.67	10.1	2.67	1.27	0.12	21.7	0.22	55	6.06	15.8	4.71	39.8	9.48	1.37	-0.03
RJS 6	66	8.98	4.17	10.6	2.42	1.16	0.15	22.3	0.33	56	5.87	18.6	4.94	39.1	10.4	1.58	-0.75
RJS 7	78	8.41	5.43	8.48	2.89	1.52	0.22	23.1	0.26	48	6.36	192	5.44	33.3	10.6	1.45	0.45
RJS 8	87	8.43	5.53	9.05	2.95	1.52	0.13	23.1	0.21	47	5.03	14.4	4.39	35.4	8.81	1.15	0.23
RJS 9	99	8.33	6.27	8.69	3.36	1.68	0.13	23.3	0.18	44	5.13	14.2	4.37	32.8	8.68	1.21	0.74
RJS 10	110	8.35	5.67	9.07	3.00	1.58	0.15	23.5	0.18	47	4.94	13.9	4.25	34.8	8.54	1.30	0.02
RJS 11	124	8.25	5.70	8.53	2.94	1.57	0.19	23.9	0.15	46	5.24	14.1	4.29	31.0	8.32	1.42	-0.11
RJS 12	235	8.30	5.97	8.84	3.17	1.68	0.14	23.6	0.19	45	5.22	14.9	4.61	32.3	9.01	1.09	0.34
RJS 13	247	7.89	7.45	7.98	3.91	1.93	0.14	23.7	0.13	39	4.60	12.6	4.12	31.4	7.19	0.85	1.19
RJS 14	269	7.82	7.63	8.41	3.94	2.05	0.17	24.4	0.14	38	4.89	13.4	4.28	31.9	7.56	0.83	1.86
RJS 15	296	7.76	7.64	8.27	3.91	2.45	0.20	23.9	0.13	37	4.60	12.6	4.06	32.2	6.98	0.82	1.33
RJS 16 (parent)	376	7.70	7.17	8.37	3.83	2.02	0.32	24.0	0.14	39	4.89	13.0	4.23	31.5	7.56	0.84	1.19
Pakuria profile (PP)																	
PA1	50	8.96	0.34	15.8	0.39	0.12	0.38	20.3	0.29	91	11.83	29.8	5.12	32.0	22.4	10.14	NA
PB1	90	9.91	2.02	8.67	1.10	0.47	0.16	20.4	0.19	75	6.70	24.0	6.63	47.8	17.3	1.83	-0.69
PB2	125	9.49	4.15	7.31	1.60	1.25	0.22	22.4	0.11	57	5.57	13.0	4.03	42.5	8.06	1.04	0.76
PB3	165	9.17	2.49	8.55	1.23	0.75	0.20	21.1	0.19	68	6.24	18.4	4.94	44.0	11.1	1.65	-1.04
PB4	225	9.00	6.13	7.46	2.25	1.84	0.28	23.2	0.12	46	5.04	12.0	4.01	40.5	7.14	0.75	1.79
PB5	290	8.76	5.81	7.76	2.15	1.67	0.22	22.9	0.10	47	5.27	12.7	4.09	40.7	7.08	0.72	1.81
PERN	325	8.67	7.14	7.46	2.44	2.31	0.27	23.5	0.12	41	4.97	11.9	3.81	37.0	6.49	0.66	2.03
PFAA	625	9.30	7.00	6.59	2.23	2.58	0.34	24.0	0.10	42	4.92	12.3	4.00	36.7	6.83	0.67	2.17
PFB1 (parent)	1000	8.71	7.40	7.40	2.85	2.42	0.22	23.3	0.12	40	4.75	11.9	3.79	37.8	6.42	0.65	2.45

*CIA values were calculated using the molar proportions of the oxides. $\text{CIA} = [\text{Al}_2\text{O}_3 / (\text{Al}_2\text{O}_3 + \text{CaO} + \text{Na}_2\text{O} + \text{K}_2\text{O})] \times 100$.

$\epsilon_{Nd}^{\#} = \{[(^{143}\text{Nd}/^{144}\text{Nd})_{\text{sample}} / (^{143}\text{Nd}/^{144}\text{Nd})_{\text{CHUR}}] - 1\} \times 10^4$, where $(^{143}\text{Nd}/^{144}\text{Nd})_{\text{CHUR}} = 0.512638$ (Jacobsen and Wasserburg, 1980).

Supplementary Table ST2. Immobile elemental ratios of parent basalts and weathering profiles.

Profile	Sample code	Nb/Al (mass ratio)	Th/Al (mass ratio)
Dalahi	RJS 1-2	0.85-0.88	0.29-0.38
	RJS 3-15	0.64±0.04	0.14±0.03
	RJS 16 (parent)	0.64	0.11
Pakuria	PA1	1.32	1.13
	PB1-PFAA	0.59±0.06	0.11±0.05
	PFB1 (parent)	0.54	0.07

The codes, depth in the profiles, and the concentrations of Al, Nb and Th for individual samples are listed in Supplementary Table ST1.

Supplementary Table ST3. The composition of the oxyhydroxide and exchangeable phases. The calculated ϵ_{Nd} values of the residual phases and the ϵ_{Nd} difference between the parent basalt and residual phases are also given.

Sample code	Depth (cm)	Exchangeable		Oxyhydroxides			Nd _{Res} (%) [*]	ϵ_{Nd}^{Res}	$\Delta\epsilon_{Nd}^{P-Res}$
		Mn	Nd	Mn	Nd	ϵ_{Nd}^{Ox}			
		$\mu\text{g/g}$		$\mu\text{g/g}$					
Dalahi profile (DP)									
RJS 3	32	40.8	0.29	992	0.33	2.57	98	-1.18	2.37
RJS 4	43	16.2	0.18	1138	0.77	3.30	96	-0.65	1.84
RJS 5	53	26.1	0.17	550	0.40	15.3	97	-0.43	1.62
RJS 6	66	14.0	0.16	1115	0.35	9.21	98	-0.94	2.14
RJS 7	78	8.34	0.14	787	0.44	12.2	98	0.18	1.02
RJS 8	87	15.0	0.14	487	0.41	1.17	97	0.20	0.99
RJS 9	99	9.66	0.10	298	0.28	6.32	98	0.62	0.57
RJS 10	110	20.9	0.15	309	0.47	4.95	97	-0.16	1.35
RJS 11	124	22.9	0.14	232	0.24	1.39	98	-0.14	1.33
RJS 12	235	15.2	0.13	388	0.24	9.97	98	0.18	1.01
RJS 13	247	6.38	0.03	19.7	0.46	1.30	96	1.19	0.00
RJS 14	269	1.50	0.03	3.15	0.49	1.49	96	1.88	-0.68
RJS 15	296	2.75	0.02	8.51	0.35	1.38	97	1.33	-0.14
RJS 16 (parent)	376	1.80	0.02	6.91	0.42	1.76	97	1.17	0.02
Pakuria profile (PP)									
PB1	90	4.57	1.00	829	3.75	2.11	84	-1.21	3.66
PB2	125	9.75	0.30	298	2.23	3.70	83	0.15	2.30
PB3	165	2.98	0.48	780	2.21	1.65	88	-1.41	3.87
PB4	225	6.84	0.12	147	3.12	4.45	74	0.85	1.60
PB5	290	5.71	0.13	156	2.60	4.69	80	1.07	1.38
PERN	325	2.46	0.03	82.8	1.64	4.87	86	1.58	0.88
PFAA	625	0.87	0.05	15.1	0.59	4.52	95	2.05	0.40
PFB1 (parent)	1000	6.11	0.03	10.4	0.30	4.78	97	2.39	0.06

*Fraction of Nd in residual weathered phases = $\{(1 - [\text{Nd}]_{\text{ox}} / [\text{Nd}]_{\text{bulk}}) \times 100\}$, where ox and bulk represent oxyhydroxide and bulk phases, respectively. $[\text{Nd}]_{\text{bulk}}$ values are in Supplementary Table ST1

See Supplementary Note SN4 for the determination of ϵ_{Nd} of residual phase (ϵ_{Nd}^{Res}).

Supplementary Table ST4. Mean particulate ϵ_{Nd} values and discharge of global rivers during low and high flow periods.

River Name	Station Name	Length (km) ^{&}	Average ϵ_{Nd}				$\Delta\epsilon_{Nd}^{LQ-HQ}$	$\pm 2\sigma$	Average discharge $\times 10^3$ (m ³ /s)		Discharge contrast (Q _c) (%) [*]	ϵ_{Nd} and discharge data source
			High discharge		Low discharge				High discharge (HQ)	Low discharge (LQ)		
			ϵ_{Nd}^{HQ}	$\pm 2\sigma$	ϵ_{Nd}^{LQ}	$\pm 2\sigma$						
Time Series Data												
Amazon	Obidos	3869	-11.00	0.07	-10.06	0.09	0.94	0.11	244 \pm 12	88 \pm 7	64	Rousseau et al. 2019
Orinoco	Ciudad bolivar	1570	-14.17	0.06	-13.72 ⁽ⁱ⁾	0.05	0.45	0.08	66 \pm 4	11 \pm 6	84	Rousseau et al. 2019
Maroni	Langa Tabiki	389	-24.87	0.09	-22.80 ⁽ⁱⁱ⁾	0.09	2.07	0.13	4.2 \pm 0.4	0.9 \pm 0.4	78	Rousseau et al. 2019
Solimoes [#]	Manacapuru	1996	-9.39	0.10	-9.09 ⁽ⁱ⁾	0.06	0.30	0.11	126 \pm 1	80 \pm 0.3	30	Viers et al. 2008
Madeira [#]	Porto Velho	1869	-12.01 ⁽ⁱ⁾	0.05	-11.27	0.08	0.74	0.09	24 \pm 1	5 \pm 2	78	Viers et al. 2008
Tumbes (2007-2008)	El Tigre	182	-6.36	0.12	-3.42	0.07	2.94	0.14	0.117 \pm 0.053	0.015 \pm 0.002	88	Moquet et al. 2020
Tumbes (2010-2011)	El Tigre	182	-6.30	0.08	-3.45 ⁽ⁱⁱ⁾	0.05	2.84	0.09	0.327 \pm 0.055	0.026 \pm 0.014	92	Moquet et al. 2020
Minjiang	S04	685	-11.82	0.21	-10.71	0.07	1.11	0.23	4.4	0.9 \pm 0.8	79	Jian et al. 2020b
Changjiang	Nanjing	4429	-10.96	0.10	-11.79	0.08	-0.84	0.13	44 \pm 4	13 \pm 2	70	Mao et al. 2011
Seasonal discrete data												
Ganga	Harding bridge	1993	-18.49		-17.95		0.54		41.5	18.0	57	Lupker et al. 2011;2013
Brahmaputra [§]	Guwahati	1974	-12.79		-12.50		0.29		38.5	20.2	48	Singh et al. 2002
Changjiang	Datong	4279	-14.75	0.15	-13.42	0.10	1.33	0.18	62.9	43.3	31	Luo et al. 2012
Parana [§]	Rosario	3580	-10.30	0.18	-11.20	0.18	-0.90	0.25	15.5	12.0	23	Henry et al. 1996
Uruguay [§]	Gualeguaychu	1710	-6.70	0.18	-6.00	0.18	0.70	0.25	7.3	4.6	37	Henry et al. 1996
Amazon [#]	Obidos	3869	-10.30	0.18	-10.12	0.25	0.18	0.31	255	118	54	Merschel et al. 2017
Tapajos [#]	Alter do Chao	2218	-18.79	0.14	-19.33	0.39	-0.55	0.41	10.3	7.6	26	Merschel et al. 2017
Xingu [#]	Porto de Moz	2060	-25.05	0.39	-22.53	0.33	2.52	0.51	5.5	1.8	66	Merschel et al. 2017

[&]River length from the origin, sourced from [UNH/GRDC Composite Runoff Fields V1.0](#).

^{*}Discharge contrast (Q_c) = [(HQ-LQ) \times 100/HQ].

[#]Discharge data from HyBam research program (<http://www.ore-hybam.org>).

[§]River water discharge data from [UNH/GRDC Composite Runoff Fields V1.0](#).

⁽ⁱ⁾Two outliers excluded. ⁽ⁱⁱ⁾One outlier excluded.

Calculations of ϵ_{Nd} and discharge mean for the HQ and LQ periods are explained in Supplementary Note SN6.

Supplementary Table ST5. Results of regression analysis of particulate ϵ_{Nd} vs. discharge of time series data.

River	Range of ϵ_{Nd}	r	p	n
Tumbes (2007-2008)	-7.76 to -1.89	-0.71	0.01	11
Tumbes (2010-2011) ^s	-6.70 to -2.42	-0.76	0.01	11
Amazon	-11.41 to -9.77	-0.77	0.003	12
Orinoco [*]	-14.55 to -13.71	-0.65	0.05	9
Maroni [@]	-25.20 to -21.20	-0.76	0.02	9
Madeira ^{&}	-12.11 to -10.85	-0.66	0.04	10
Solimoes [#]	-9.87 to -8.93	-0.58	0.1	8
Minjiang	-11.8 to -10.2	-0.69	0.01	13
Changjiang	-12.07 to -10.55	0.77	0.002	13

r=correlation coefficient, **p**=confidence limit and **n**=number of data points that were subject to regression.

The outliers excluded from the regression analysis: ^sOne outlier of lean flow period. ^{*}Two outliers of lean flow period. [@]One outlier each for the lean and peak flow period. [&]Two outliers of peak flow period. [#]Two outliers of lean and one outlier of peak flow period.

Data sources given in Supplementary Table ST4.

Supplementary References

- Aydin, O., Yassikaya, M. Y., 2022. Validity and reliability analysis of the PlotDigitizer software program for data extraction from single-case graphs. *Perspectives on Behavior Science* 45, 239-257. <https://doi.org/10.1007%2Fs40614-021-00284-0>
- Baksi, A. K., 2022. Geochemistry and geochronology of the Rajmahal Flood Basalt Province, northeastern India: Genetic links to Kerguelen hotspot activity. *Journal of Earth System Science* 131, 157. <https://doi.org/10.1007/s12040-022-01855-8>
- Bhattacharyya, R., Singh, S. P., Qasim, A., Chandrashekhar, A. K., 2024. Geochemical and radiogenic Sr-Nd isotope characterization of widespread sandy surface sediments in the Great Indian Desert, Thar: Implications for provenance studies. *Journal of Geophysical Research: Earth Surface* 129(8), e2023JF007625. <https://doi.org/10.1029/2023JF007625>
- Chatterjee, J., Singh S. K., 2014. Dissolved Nd in the Ganga River system and its flux to the Bay of Bengal, Goldschmidt. <https://goldschmidtabstracts.info/2014/387.pdf>
- Chauvel, C., Garçon, M., Bureau, S., Besnault, A., Jahn, B. M., Ding, Z., 2014. Constraints from loess on the Hf-Nd isotopic composition of the upper continental crust. *Earth and Planetary Science Letters*, 388 48-58. <https://doi.org/10.1016/j.epsl.2013.11.045>
- Galy, A., France-Lanord, C., Hurtrez, J. E., 1998. Distribution of physical erosion in Himalaya from river particle geochemistry. *Mineralogical Magazine* 62, 493-494. <http://dx.doi.org/10.1180/minmag.1998.62A.1.261>
- Ghose, N. C., Chatterjee, N., Windley, B. F., 2017. Subaqueous Eruptive Phase of the Late Aaptian Rajmahal Volcanism India: Evidence from Volcaniclastic Rocks, Bentonite, Black Shales and Oolite. *Geoscience Frontiers* 8, 809-822. <https://doi.org/10.1016/j.gsf.2016.06.007>
- Ghosh, S., Guchhait, S. K., 2015 Characterization and evolution of primary and secondary laterites in northwestern Bengal Basin, West Bengal, India. *Journal of Palaeogeography* 4, 203-230. <https://doi.org/10.3724/SP.J.1261.2015.00074>
- Ghosh, S., Guchhait, S. K., 2019. Modes of formation, palaeogene to early quaternary palaeogenesis and geochronology of laterites in rajmahal basalt traps and Rarh Bengal of Lower Ganga Basin. *Quaternary Geomorphology in India: Case Studies from the Lower Ganga Basin*, 25-60. https://doi.org/10.1007/978-3-319-90427-6_2
- Henry, F., Probst, J. L., Thouron, D., Depetris, P., Garçon, V., 1996. Nd-Sr isotopic compositions of dissolved and particulate material transported by the Parana and Uruguay rivers during high (December 1993) and low (September 1994) water periods. *Geological Sciences, Bulletins and Memoirs* 49, 89-100.
- Hindshaw, R. S., Aciego, S. M., Piotrowski, A. M., Tipper, E. T., 2018b. Decoupling of dissolved and bedrock neodymium isotopes during sedimentary cycling. *Geochemical Perspectives Letters* 8, 43-46. <https://doi.org/10.7185/geochemlet.1828>
- Hindshaw, R. S., Tosca, N. J., Piotrowski, A. M., Tipper, E. T., 2018a. Clay mineralogy, strontium and neodymium isotope ratios in the sediments of two High Arctic catchments (Svalbard). *Earth Surface Dynamics* 6, 141-161. <https://doi.org/10.5194/esurf-6-141-2018>
- Jacobsen, S. B., Wasserburg, G. J., 1980. Sm-Nd isotopic evolution of chondrites. *Earth and Planetary Science Letters* 50, 139-155. [https://doi.org/10.1016/0012-821X\(80\)90125-9](https://doi.org/10.1016/0012-821X(80)90125-9)

- Jian, X., Yang, S., Hong, D., Liang, H., Zhang, S., Fu, H., Zhang, W., 2020a. Seasonal geochemical heterogeneity of sediments from a subtropical mountainous river in SE China. *Marine Geology* 422, 106120. <https://doi.org/10.1016/j.margeo.2020.106120>
- Jian, X., Zhang, W., Yang, S., Kao, S. J., 2020b. Climate-dependent sediment composition and transport of mountainous rivers in tectonically stable, subtropical East Asia. *Geophysical Research Letters* 47, e2019GL086150. <https://doi.org/10.1029/2019GL086150>
- Larkin, C.S., Piotrowski, A.M., Hindshaw, R.S., Bayon, G., Hilton, R.G., Baronas, J.J., Dellinger, M., Wang, R., Tipper, E.T., 2021. Constraints on the source of reactive phases in sediment from a major Arctic River using neodymium isotopes. *Earth and Planetary Science Letters* 565, p.116933. <https://doi.org/10.1016/j.epsl.2021.116933>
- Luo, C., Zheng, H., Wu, W., Wang, P., Chen, Y., Wei, X., 2012. Sr-Nd isotope stratification along water depth: An example from Datong hydrological station of Yangtze River. *Chinese Science Bulletin* 57, 4482-4490. <https://doi.org/10.1007/s11434-012-5311-z>
- Lupker, M., France-Lanord, C., Galy, V., Lavé, J., Kudrass, H., 2013. Increasing chemical weathering in the Himalayan system since the Last Glacial Maximum. *Earth and Planetary Science Letters* 365, 243-252. <https://doi.org/10.1016/j.epsl.2013.01.038>
- Lupker, M., France-Lanord, C., Lavé, J., Bouchez, J., Galy, V., Métivier, F., Gaillardet, J., Lartiges, B., Mugnier, J. L., 2011. A Rouse-based method to integrate the chemical composition of river sediments: Application to the Ganga basin. *Journal of Geophysical Research: Earth Surface*, 116(F4). <https://doi.org/10.1029/2010JF001947>
- Ma, J. L., Wei, G. J., Xu, Y. G., Long, W. G., Sun, W. D., 2007. Mobilization and re-distribution of major and trace elements during extreme weathering of basalt in Hainan Island, South China. *Geochimica et Cosmochimica Acta* 71(13), 3223-3237. <https://doi.org/10.1016/j.gca.2007.03.035>
- Mao, C., Chen, J., Yuan, X., Yang, Z., Balsam, W., Ji, J., 2010. Seasonal variation in the mineralogy of the suspended particulate matter of the lower Changjiang River at Nanjing, China. *Clays and Clay Minerals* 58, 691-706. <https://doi.org/10.1346/CCMN.2010.0580508>
- Mao, C., Chen, J., Yuan, X., Yang, Z., Ji, J., 2011. Seasonal variations in the Sr-Nd isotopic compositions of suspended particulate matter in the lower Changjiang River: Provenance and erosion constraints. *Chinese Science Bulletin* 56, 2371-2378. <https://doi.org/10.1007/s11434-011-4589-6>
- Maynard, J. B., 1992. Chemistry of modern soils as a guide to interpreting Precambrian paleosols. *The Journal of Geology* 100, 279-289. <https://doi.org/10.1086/629632>
- Merschel, G., Bau, M., Schmidt, K., Münker, C., Dantas, E. L., 2017. Hafnium and neodymium isotopes and REY distribution in the truly dissolved, nanoparticulate/colloidal and suspended loads of rivers in the Amazon Basin, Brazil. *Geochimica et Cosmochimica Acta* 213, 383-399. <https://doi.org/10.1016/j.gca.2017.07.006>
- Moquet, J.S., Morera, S., Turcq, B., Poitrasson, F., Roddaz, M., Moreira-Turcq, P., Espinoza, J.C., Guyot, J.L., Takahashi, K., Orrillo-Vigo, J., Petrick, S., Mounic, S., Sondag, F., 2020. Control of seasonal and inter-annual rainfall distribution on the Strontium-Neodymium isotopic compositions of suspended particulate matter and implications for tracing ENSO events in the Pacific coast (Tumbes basin, Peru). *Global and Planetary Change* 185, 103080. <https://doi.org/10.1016/j.gloplacha.2019.103080>

- Mukherjee, P. K., 1971. Petrology of Rajmahal Traps of the NW Rajmahal Hills, India. *Bulletin of Volcanology* 35, 887-906. <https://doi.org/10.1007/BF02596853>
- Nesbitt, H. W., Markovics, G., 1997. Weathering of granodioritic crust, long-term storage of elements in weathering profiles, and petrogenesis of siliciclastic sediments. *Geochimica et Cosmochimica Acta* 61, 1653-1670. [https://doi.org/10.1016/S0016-7037\(97\)00031-8](https://doi.org/10.1016/S0016-7037(97)00031-8)
- Rousseau, T. C., Roddaz, M., Moquet, J. S., Delgado, H. H., Calves, G., Bayon, G., 2019. Controls on the geochemistry of suspended sediments from large tropical South American rivers (Amazon, Orinoco and Maroni). *Chemical Geology* 522, 38-54. <https://doi.org/10.1016/j.chemgeo.2019.05.027>
- Singh, S. K., France-Lanord, C., 2002. Tracing the distribution of erosion in the Brahmaputra watershed from isotopic compositions of stream sediments. *Earth and Planetary Science Letters* 202, 645-662. [https://doi.org/10.1016/S0012-821X\(02\)00822-1](https://doi.org/10.1016/S0012-821X(02)00822-1)
- Tachambalath, A. P., France-Lanord, C., Galy, A., Rigaudier, T., Charreau, J., 2023. Data report: major and trace element composition of silicates and carbonates from Bengal Fan sediments, IODP Expedition 354. <https://doi.org/10.14379/iodp.proc.354.204.2023>
- Taylor, S.R., McLennan, S.M., 1985. *The Continental Crust: Its Composition and Evolution*. Blackwell, Oxford, UK, 349.
- Tricca, A., Stille, P., Steinmann, M., Kiefel, B., Samuel, J., Eikenberg, J., 1999. Rare earth elements and Sr and Nd isotopic compositions of dissolved and suspended loads from small river systems in the Vosges mountains (France), the river Rhine and groundwater. *Chemical Geology* 160, 139-158. [https://doi.org/10.1016/S0009-2541\(99\)00065-0](https://doi.org/10.1016/S0009-2541(99)00065-0)
- Viers, J., Roddaz, M., Filizola, N., Guyot, J.L., Sondag, F., Brunet, P., Zouiten, C., Boucayrand, C., Martin, F., Boaventura, G.R., 2008. Seasonal and provenance controls on Nd–Sr isotopic compositions of Amazon rivers suspended sediments and implications for Nd and Sr fluxes exported to the Atlantic Ocean. *Earth and Planetary Science Letters* 274, 511-523. <https://doi.org/10.1016/j.epsl.2008.08.011>
- Wang, Z., Ma, J., Li, J., Wei, G., Zeng, T., Li, L., Zhang, L., Deng, W., Xie, L., Liu, Z., 2018. Fe (hydro) oxide controls Mo isotope fractionation during the weathering of granite. *Geochimica et Cosmochimica Acta*, 226 1-17. <https://doi.org/10.1016/j.gca.2018.01.032>
- Yuan, W., Gong, Y., Chen, J., Wang, Z., Huang, F., Yang, X., Chetelat, B., Teng, H., Schott, J., 2022. Gallium isotope constraints on the intense weathering of basalt. *Geochimica et Cosmochimica Acta*, 333 22-38. <https://doi.org/10.1016/j.gca.2022.06.042>